

## Construction and application of multi-element EAM potential (Ni–Al–Re) in $\gamma$ Ni-based single crystal superalloys

This article has been downloaded from IOPscience. Please scroll down to see the full text article.

2013 Modelling Simul. Mater. Sci. Eng. 21 015007

(<http://iopscience.iop.org/0965-0393/21/1/015007>)

View [the table of contents for this issue](#), or go to the [journal homepage](#) for more

Download details:

IP Address: 114.251.50.252

The article was downloaded on 18/12/2012 at 23:39

Please note that [terms and conditions apply](#).

# Construction and application of multi-element EAM potential (Ni–Al–Re) in $\gamma/\gamma'$ Ni-based single crystal superalloys

J P Du<sup>1</sup>, C Y Wang<sup>1,2,3</sup> and T Yu<sup>1</sup>

<sup>1</sup> Central Iron and Steel Research Institute, Beijing 100081, People's Republic of China

<sup>2</sup> Department of Physics, Tsinghua University, Beijing 100084, People's Republic of China

<sup>3</sup> The International Center for Materials Physics, Chinese Academy of Sciences, Shenyang 110016, People's Republic of China

E-mail: [cywang@mail.tsinghua.edu.cn](mailto:cywang@mail.tsinghua.edu.cn)


Received 5 August 2012, in final form 31 October 2012

Published 18 December 2012

Online at [stacks.iop.org/MSMSE/21/015007](http://stacks.iop.org/MSMSE/21/015007)

## Abstract

Based on experiments and first-principles calculations, a Ni–Al–Re system embedded atom method (EAM) potential is constructed for the  $\gamma(\text{Ni})/\gamma'(\text{Ni}_3\text{Al})$  superalloy. The contribution of the inner elastic constants is considered in the fitting of Re with a hexagonal close-packed structure. Using this potential, point defects, planar defects and lattice misfit of  $\gamma(\text{Ni})$  and  $\gamma'(\text{Ni}_3\text{Al})$  are investigated. The interaction between Re and the misfit dislocation of the  $\gamma(\text{Ni})/\gamma'(\text{Ni}_3\text{Al})$  system is also calculated. We conclude that the embedding energy has an important effect on the properties of the alloys, such as the planar fault energies of  $\text{Ni}_3\text{Al}$ , by considering the relationship between the charge transfer calculated from first-principles, the elastic constants of  $\text{Ni}_3\text{Al}$  and the host electron density of the EAM potential. The multi-element potential predicts that Re does not form clusters in  $\gamma(\text{Ni})$ , which is consistent with recent experiments and first-principles calculations.

 Online supplementary data available from [stacks.iop.org/MSMSE/21/015007/mmedia](http://stacks.iop.org/MSMSE/21/015007/mmedia)

(Some figures may appear in colour only in the online journal)

## 1. Introduction

Ni-based single crystal superalloys, characterized by a high volume fraction of the cubic  $\gamma'$  phase embedded in the  $\gamma$  matrix phase, are widely used for turbine blades in gas turbine engines. The mechanical properties of the superalloys have been significantly improved by the addition of Re in second and third generation superalloys [1–3]. However, the mechanism of Re on the improvement of the mechanical properties is still not well understood. Atom probe

and field ion microscope experiments have revealed that Re mainly partitions to the  $\gamma$  matrix and has a tendency to form clusters [4–6]. Thus, the mechanical property of the superalloys is improved by Re clusters retarding the coarsening of the  $\gamma'$  phase and the motion of the matrix dislocations. However, Mottura *et al* [7–9] experimentally found that Re does not form clusters in the Ni–Re binary alloy and  $\gamma$  phase of the superalloys using the local electrode atom probe, atom probe tomography and the extended x-ray absorption fine structure technique. Based on these experiments, further theoretical and experimental investigations are needed to study the rhenium effect, especially the influence of Re on the dislocation motion.

In recent years, considerable effort has been made to understand the alloying effects and partitioning behavior of Re on the  $\gamma(\text{Ni})/\gamma'(\text{Ni}_3\text{Al})$  interface using first-principles calculations [10–12]. However, first-principles simulations are limited to a few hundred atoms and many properties need to be studied at the atomic level using empirical potentials, especially for dislocation motion and crack propagation [13–17]. Interatomic potentials are crucial for the credibility of atomic simulations. Mottura *et al* [18] suggested that the modified analytical embedded atom method (EAM) potential used in [19] does not model the behavior of diluted Re atoms in  $\gamma(\text{Ni})$  reliably. Thus, reliable multi-element Ni–Al–X (X denotes alloying elements such as Re, Ru and Cr) potentials are necessary for the superalloys. The EAM [20, 21] has been successfully used to model the structure of various defects in monoatomic metals and binary alloys. EAM potentials have been constructed for Ni and Ni<sub>3</sub>Al [22–25], but multi-element potentials containing Re still need to be constructed. To obtain the Ni–Al–Re analytic potential in this work, we have constructed the ternary potential based on the EAM potential developed by Cai and Ye [26] (Cai–Ye potential). The Cai–Ye potential gives a reasonable description of both bulk and surface properties for face centered cubic (fcc) metals. For cross-potentials of binary alloys, Cai and Ye assumed the density-weighted combination of monoatomic pair potentials [27] fitting to the dilute-limit heat of solution. However, fitting of the planar fault energies of Ni<sub>3</sub>Al, such as the complex stacking fault (CSF) and the antiphase boundary (APB) fault, often needs more parameters in the cross-potential than the density-weighted combination. Thus, the pair potential of the Cai–Ye EAM potential is modified in this study. In the construction of the present potential, we laid special emphasis on the effect of the many-body term or the embedding energy term of the EAM on the alloy properties, especially the planar faults of Ni<sub>3</sub>Al. The parameters of the potential related to the atomic electron density should be considered in the numerical fitting of the potentials based on the charge transfer between the elements. The effects of Re on the  $\gamma(\text{Ni})$ ,  $\gamma'(\text{Ni}_3\text{Al})$  and  $\gamma(\text{Ni})/\gamma'(\text{Ni}_3\text{Al})$  interface are investigated to ensure that the potential can be used to model the behavior of Re in the  $\gamma(\text{Ni})/\gamma'(\text{Ni}_3\text{Al})$  system.

Here, we construct the ternary Ni–Al–Re potential to study the effect of Re on the properties of the  $\gamma(\text{Ni})/\gamma'(\text{Ni}_3\text{Al})$  superalloy. This paper is arranged as follows. Section 2 introduces the expression of the EAM model and the construction of the potential. The results of the current potential for lattice properties, point defects and planar defect properties in the  $\gamma(\text{Ni})/\gamma'(\text{Ni}_3\text{Al})$  system are demonstrated in section 3. A discussion on the effect of embedding energy on the properties of Ni<sub>3</sub>Al is demonstrated in section 4. The final section gives our major conclusions.

## 2. Construction of the potentials

### 2.1. Parameterizations of potential functions

In the scheme of the EAM [20, 21], the total energy  $E_{\text{tot}}$  of the system of  $N$  atoms is written as

$$E_{\text{tot}} = \sum_i F(\rho_i) + \sum_{i>j} \phi(r_{ij}), \quad (1)$$

where  $F(\rho_i)$  is the embedding energy of atom  $i$ ,  $\phi(r_{ij})$  is the two-body potential between atoms  $i$  and  $j$ ,  $\rho_i$  is the host electron density at atom  $i$  contributed by the other atoms and  $r_{ij}$  is the distance between atoms  $i$  and  $j$ . According to the linear superposition approximation the host electron density  $\rho_i$  is given by

$$\rho_i = \sum_j f(r_{ij}). \quad (2)$$

Here  $f(r_{ij})$  is the electron density of atom  $j$ . For a ternary system Ni–Al–Re, the 12 potential functions, namely  $F_{\text{Ni}}(\rho)$ ,  $F_{\text{Al}}(\rho)$ ,  $F_{\text{Re}}(\rho)$ ,  $f_{\text{Ni}}(r)$ ,  $f_{\text{Al}}(r)$ ,  $f_{\text{Re}}(r)$ ,  $\phi_{\text{NiNi}}(r)$ ,  $\phi_{\text{AlAl}}(r)$ ,  $\phi_{\text{ReRe}}(r)$ ,  $\phi_{\text{NiAl}}(r)$ ,  $\phi_{\text{NiRe}}(r)$  and  $\phi_{\text{AlRe}}(r)$ , must be obtained. In these 12 potential functions the monoatomic potentials of Ni, Al and Re are fitted to the experimental properties separately, then the pair potential  $\phi_{\text{NiAl}}(r)$  is fitted to the experimental properties of  $\text{Ni}_3\text{Al}$ , and finally the pair potentials  $\phi_{\text{NiRe}}(r)$  and  $\phi_{\text{AlRe}}(r)$  are fitted to the results of first-principles calculations.

The atomic electron density is parameterized in the form

$$f(r) = s \tilde{f}(r) \Psi\left(\frac{r - r_c}{h}\right), \quad (3)$$

$$\tilde{f}(r) = f_e \exp[-\chi(r - r_e)], \quad (4)$$

where  $s$  is a parameter,  $\tilde{f}(r)$  is the atomic electron density used by Cai and Ye [26] and  $\Psi((r - r_c)/h)$  is a cutoff function defined as [28]

$$\Psi(x) = \begin{cases} \frac{x^4}{1 + x^4}, & x < 0, \\ 0, & x \geq 0. \end{cases} \quad (5)$$

The parameters  $f_e$ ,  $\chi$  and  $r_e$  are determined by using  $\tilde{f}(r)$  to fit the atomic electron density calculated using the first-principles code Dmol3 [29, 30]. The fitting results are shown in the inset of figure 1(a). It can be seen from figure 1(a) that the atomic electron density from first-principles calculations can be expressed as an exponential function.  $r_c$  and  $h$  are parameters that are obtained in the fitting of monoatomic potentials.

The embedding energy and pair potential of Cai and Ye [26] are given by the equations

$$F(\rho) = -F_0 \left[ 1 - \ln\left(\frac{\rho}{\rho_e}\right)^n \right] \left(\frac{\rho}{\rho_e}\right)^n + F_1 \frac{\rho}{\rho_e}, \quad (6)$$

and

$$\phi(r) = -\alpha [1 + \beta(r/r_0 - 1)] \exp[-\beta(r/r_0 - 1)], \quad (7)$$

where  $F_0 = E_c - E_v^f$ ,  $E_c$  and  $E_v^f$  are the cohesive energy and the vacancy formation energy, respectively.  $n$  equals 0.5 and  $\rho_e$  is the host electron density of the atom in the equilibrium lattice structure. The cutoff distance is set to  $1.65a_0$ , where  $a_0$  is the equilibrium lattice constant.

In this work, the embedding energy was taken from the expression given by Banerjee and Smith [31]

$$F(\rho) = -F_0 \left[ 1 - \ln\left(\frac{\rho}{\rho_e}\right)^n \right] \left(\frac{\rho}{\rho_e}\right)^n. \quad (8)$$

Effective pair potentials [32] are used in this work to analyze the influence of the many-body effects on the alloy properties. Effective pair potential means that the first derivative of the embedding energy at the equilibrium host electron density is equal to zero in the monoatomic metals, i.e.  $F'(\rho_e) = 0$ . The expression for the embedding energy equation (8) satisfies this condition. In the present potential,  $F_0$  is also taken as [32]  $F_0 = E_c - E_v^f$ . The parameter  $n$

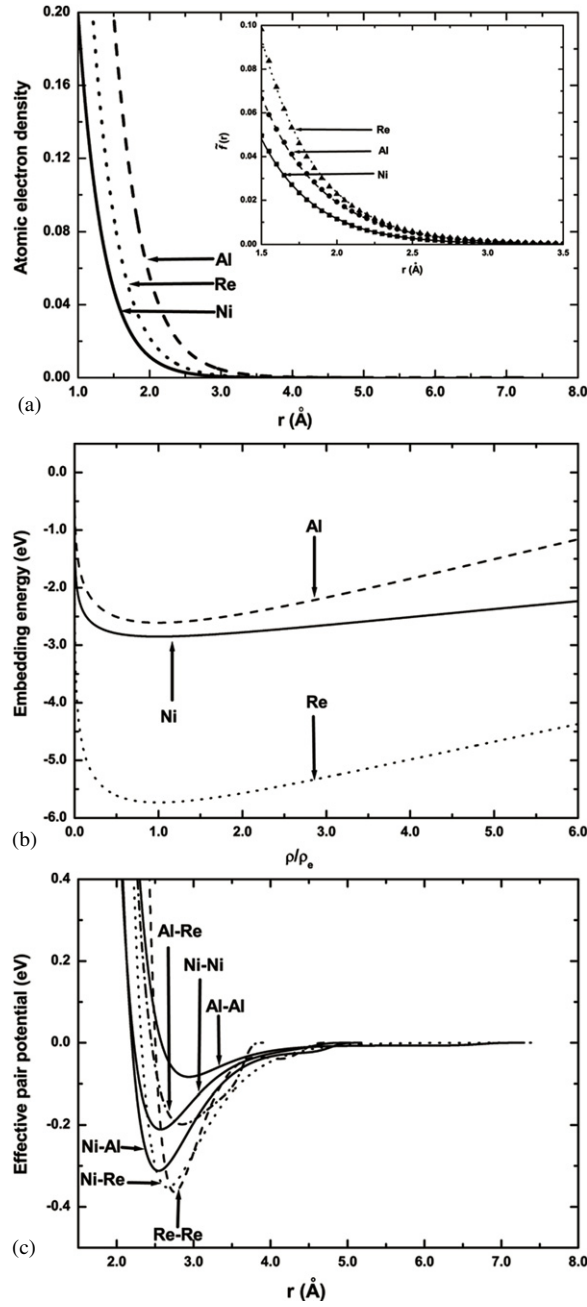


**Figure 1.** (a) Atomic electron densities for Ni, Al and Re. The inset shows the atomic electron density calculated with Dmol3 (solid symbols) and the fitted function of  $\tilde{f}(r)$  (lines). (b) Embedding energies for Ni, Al and Re. (c) Pair potentials for Ni, Al, Re and cross functions.

is an adjustable parameter. When the embedding energy is taken as a function of  $\rho/\rho_e$ , the parameter  $s$  cancels in monoatomic systems. However,  $s$  changes the energy of binary and ternary systems and it cannot be cancelled. If  $s_{\text{Ni}}$  is set to 1, then  $s_{\text{Al}}$  and  $s_{\text{Re}}$  can be used as adjustable parameters.

**Table 1.** Potential parameters of the present EAM potential for Ni, Al and Re.

Parameter	Ni	Al	Re
$f_e$	$2.81 \times 10^{-3}$	$2.23 \times 10^{-3}$	$3.04 \times 10^{-3}$
$r_e(\text{\AA})$	2.50	2.85	2.75
$\chi(\text{\AA}^{-1})$	2.8411	2.5268	2.7527
$n$	$3.0447 \times 10^{-1}$	$4.4658 \times 10^{-1}$	$3.1691 \times 10^{-1}$
$s$	1.0000	2.9236	$9.3399 \times 10^{-1}$
$\rho_e$	$3.5985 \times 10^{-2}$	$7.8227 \times 10^{-2}$	$3.2387 \times 10^{-2}$
$d_{AA}^A(\text{eV})$	$-2.3014 \times 10^1$	$1.4317 \times 10^{-1}$	$2.5718 \times 10^{-1}$
$\alpha(\text{eV})$	$1.2510 \times 10^{-2}$	$1.0034 \times 10^{-1}$	$4.3132 \times 10^{-1}$
$\beta$	$1.0000 \times 10^{-3}$	8.1857	$1.0551 \times 10^1$
$\gamma(\text{eV})$	-3.5163	$4.0514 \times 10^{-3}$	$9.5435 \times 10^{-5}$
$\kappa$	7.5831	$-5.2299 \times 10^{-1}$	$-1.5797 \times 10^1$
$r_0(\text{\AA})$	2.4890	2.8638	2.7400
$h(\text{\AA})$	$4.8984 \times 10^{-1}$	$6.4596 \times 10^{-1}$	$9.9354 \times 10^{-1}$
$r_c(\text{\AA})$	5.0338	7.2958	4.7480

The pair potential  $\phi_{AB}$  of type-A and type-B ( $A$  and  $B = \text{Ni, Al or Re}$ ) is defined as

$$\phi_{AB}(r) = \{\varphi_{AB}(r) - \gamma \exp[-\kappa(r/r_0 - 1)]\} \Psi\left(\frac{r - r_c}{h}\right), \quad (9)$$

where

$$\varphi_{AB}(r) = -\alpha[1 + \beta(r/r_0 - 1)] \exp[-\beta(r/r_0 - 1)] + d_{AB}^A s_A \tilde{f}_A(r)/\rho_e^A + d_{AB}^B s_B \tilde{f}_B(r)/\rho_e^B. \quad (10)$$

The atomic electron densities of  $A$  and  $B$  in equation (10) correspond to the linear term of  $\rho$  in the embedding energy equation (6).  $\alpha$ ,  $\beta$ ,  $\gamma$ ,  $\kappa$ ,  $d_{AB}^A$ ,  $d_{AB}^B$ ,  $h$  and  $r_c$  are parameters. The parameters  $r_0$  in  $\phi_{\text{NiNi}}(r)$ ,  $\phi_{\text{AlAl}}(r)$ ,  $\phi_{\text{ReRe}}(r)$  and  $\phi_{\text{NiAl}}(r)$  are the first nearest neighboring distance of the monoatomic metals Ni, Al, Re and  $\text{L}_{12}\text{-Ni}_3\text{Al}$ , respectively. The parameters  $r_0$  in  $\phi_{\text{NiRe}}$  and  $\phi_{\text{AlRe}}$  are adjustable parameters.

The above potential parameters are obtained by minimizing the weighted mean square deviation between the calculated and experimental or first-principles data except the parameter  $s_{\text{Al}}$ . The parameter  $s_{\text{Al}}$  is determined using a special method because it is related to the alloy properties and used to be neglected. The method that determines  $s_{\text{Al}}$  is described in section 2.2. The first-principles data used in the fit are described in section 2.3. The profiles of the pair potentials are examined after the minimization procedure to avoid oscillating curves as far as possible. The profile of the pair potential is selected to be a similar form of the Lennard-Jones [33] and Morse [34] potentials. Such a selection may avoid the overfitting of the data. The optimized parameters are listed in tables 1 and 2, respectively. Figures 1(a), (b) and (c) show the functions of  $f(r)$ ,  $F(\rho)$  and  $\phi(r)$ , respectively. The data used in the fitting of the potentials are described in section 3. The present potential has been made available in the online supplementary materials ([stacks.iop.org/MSMSE/21/015007/mmedia](http://stacks.iop.org/MSMSE/21/015007/mmedia)) with formats compatible to the molecular dynamics (MD) programs XMD [35] and LAMMPS [36].

## 2.2. Determination of parameter $s_{\text{Al}}$ for $\text{Ni}_3\text{Al}$

In  $\text{Ni}_3\text{Al}$ , the intensity of the many-body effects is influenced by the parameter  $s_{\text{Al}}$  through the embedding energy. Because the elastic constant relationship  $C_{12} - C_{44}$  of  $\text{Ni}_3\text{Al}$  is only

**Table 2.** Potential parameters of the present EAM potential for cross-potentials.

Parameter	Ni–Al	Ni–Re	Al–Re
$\alpha(\text{eV})$	$3.5442 \times 10^{-1}$	6.4864	−7.3058
$\beta$	7.2547	3.3682	3.8635
$\gamma(\text{eV})$	$1.0466 \times 10^{-3}$	$-1.0149 \times 10^2$	$3.6780 \times 10^{-5}$
$\kappa$	−3.9796	7.4559	−3.3970
$r_0(\text{\AA})$	2.5222	1.3426	1.1348
$h(\text{\AA})$	$5.1505 \times 10^{-1}$	$4.5287 \times 10^{-1}$	$2.9098 \times 10^{-1}$
$r_c(\text{\AA})$	5.1786	7.4670	3.9028
$d_{\text{NiAl}}^{\text{Ni}}(\text{eV})$	−2.1818		
$d_{\text{NiAl}}^{\text{Al}}(\text{eV})$	1.0676		
$d_{\text{NiRe}}^{\text{Ni}}(\text{eV})$		$-1.3865 \times 10^1$	
$d_{\text{NiRe}}^{\text{Re}}(\text{eV})$		$1.1504 \times 10^1$	
$d_{\text{AlRe}}^{\text{Al}}(\text{eV})$			$-2.6293 \times 10^1$
$d_{\text{AlRe}}^{\text{Re}}(\text{eV})$			$2.7830 \times 10^1$

related to  $s_{\text{Al}}$  through  $F(\rho)$  and the  $\gamma'$  phase is constituted by  $\text{Ni}_3\text{Al}$ , the parameter  $s_{\text{Al}}$  in equation (3) is given by fitting the experimental value of  $C_{12} - C_{44}$  of  $\text{Ni}_3\text{Al}$ . Figure 2(a) shows the relationship between the calculated values of  $C_{12} - C_{44}$  and  $s_{\text{Al}}$  compared with the experimental value [23]. It can be seen from figure 2(a) that the solutions of  $s_{\text{Al}}$  are 0.22 and 2.92. The selection of the solution for  $s_{\text{Al}}$  is determined by analyzing the charge transfer from first-principles calculations. Dongare *et al* [37] suggested that the charge transfer between atoms with different electronegativities is related to the host electron density in an angular dependent potential. The EAM model is related to density functional theory with certain approximations [38]. This idea should also be suitable for the host electron density of EAM. The element that gains electrons has a larger host electron density compared with its equilibrium host electron density  $\rho_e$  in a monoatomic metal. The other element that loses electrons has a lower host electron density than its  $\rho_e$ . The electron density difference for the (1 0 0) plane of  $\text{Ni}_3\text{Al}$  calculated from first principles using Dmol3 is shown in figure 2(b). The charge density difference is defined as

$$\Delta\rho(\mathbf{r}) = \rho(\mathbf{r}) - \sum_i \rho_a(\mathbf{r}), \quad (11)$$

where  $\rho(\mathbf{r})$  and  $\rho_a(\mathbf{r})$  are the electron density of the system and the neutral atom electron density from first principles, respectively. The charge partitioning between Ni and Al given by the Hirshfeld method [39] is also shown in figure 2(b). From figure 2(b), the charge transfer from Al to Ni is consistent with other first-principles results [40]. If the host electron density of the monoatomic metal at the equilibrium structure in the EAM corresponds to the electron density of the neutral atom in first-principles calculation, then  $s_{\text{Al}} = 2.92$  can be selected considering the charge transfer from Al to Ni. This selection leads to  $\rho_{\text{Ni}}/\rho_e^{\text{Ni}} > 1$  and  $\rho_{\text{Al}}/\rho_e^{\text{Al}} < 1$  in equilibrium  $\text{Ni}_3\text{Al}$ . The influence of  $s_{\text{Al}}$  on the planar fault energies of  $\text{Ni}_3\text{Al}$  is discussed in section 3.6.

For the Dmol3 calculations, the generalized gradient approximation (GGA) was used for the exchange correlation functional. The atomic orbital basis set of double numerical plus polarization and all electron calculations with a spin-restricted mode were used in the calculations. The convergence criterion for the charge density of self-consistent iterations was set to  $10^{-6}$ , and for ionic relaxation to  $10^{-2} \text{ eV \AA}^{-1}$ .

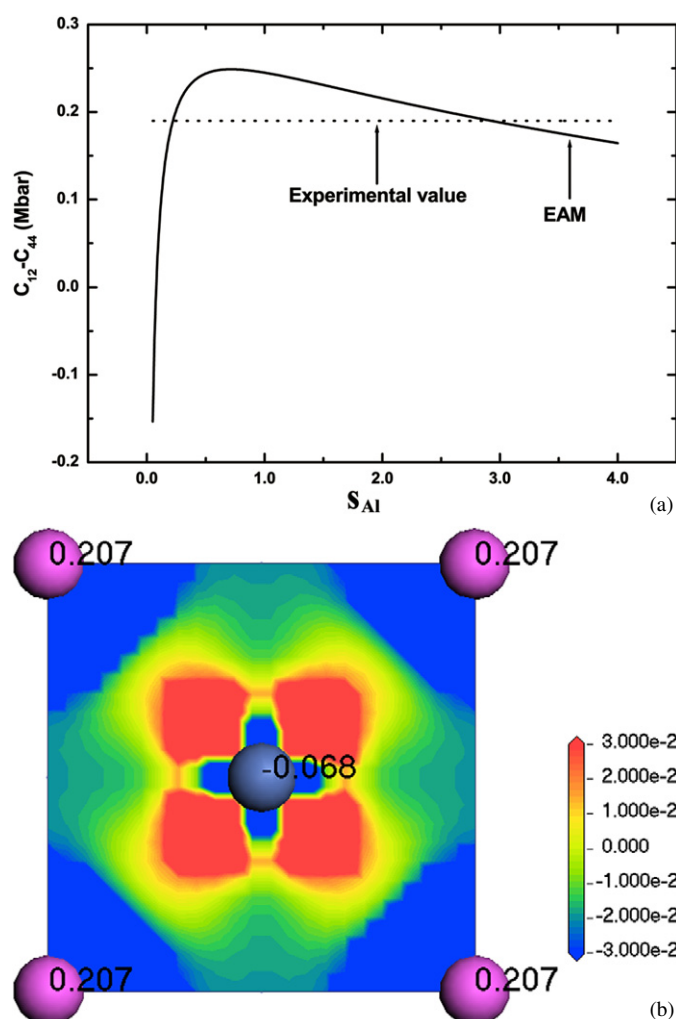


**Figure 2.** (a) Relationship between parameter  $s_{Al}$  and the calculated  $C_{12} - C_{44}$  value of  $Ni_3Al$  at the experimental lattice constant compared with the experimental value. (b) Electron density difference of the (100) plane of  $Ni_3Al$ . The blue and pink balls denote Ni and Al atoms, respectively. The charge partitioning between Ni and Al given by the Hirshfeld method is shown on the atoms.

### 2.3. Determination of potential parameters for the cross-potentials Ni–Re and Al–Re based on first-principles calculations

**2.3.1. Basic considerations for designing virtual compounds.** The alloying element Re is introduced as a substitutional solute in the superalloys. The first-principles calculations give important information on the interaction of Re–Ni and Re–Al that cannot be obtained through experiments. Considering the variation of chemical stoichiometry and environment, the fitted first-principles data include the lattice constants and the binding energies of the following ordered structures:  $L1_2$ - $Ni_3Re$ ,  $D0_{19}$ - $Ni_3Re$ ,  $D0_{22}$ - $Ni_3Re$ ,  $L1_2$ - $Re_3Al$ ,  $L1_2$ - $Al_3Re$ ,  $B_2$ - $NiRe$ ,  $B_2$ - $AlRe$  and  $L2_1$ - $Ni_2ReAl$ .

To increase the applicability of the present potential at the  $\gamma(Ni)/\gamma'(Ni_3Al)$  interface, the heats of formation of four Re-addition  $\gamma(Ni)/\gamma'(Ni_3Al)$  supercell models [11] (see figure 3)



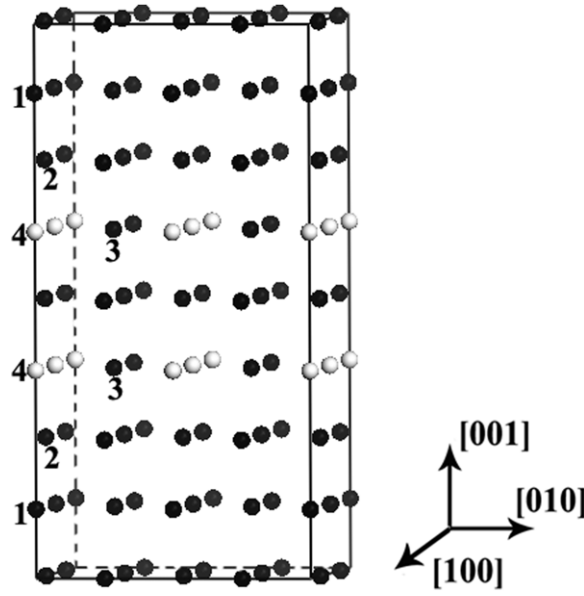


**Figure 3.** Atomic configuration of the pure and Re-addition  $\gamma(\text{Ni})/\gamma'(\text{Ni}_3\text{Al})$  interfacial models. The black and white balls denote Ni and Al atoms, respectively. The pure Ni/Ni<sub>3</sub>Al model is referred to as Noadd. The atoms labeled with 1, 2, 3 and 4 are replaced by Re in the Ni(1), Ni(2), Ni(3) and Al(4) models, respectively.

are used in the fitting. The following expression is used to calculate the heat of formation per atom of a supercell:

$$H = [E_b(n, m, l) - n \times E_b(\text{Ni}) - m \times E_b(\text{Al}) - l \times E_b(\text{Re})]/(n + m + l), \quad (12)$$

where  $E_b(n, m, l)$  is the binding energy of the supercell with  $n$ ,  $m$  and  $l$  atoms of Ni, Al and Re.  $E_b(\text{Ni})$ ,  $E_b(\text{Al})$  and  $E_b(\text{Re})$  are the binding energies per atom for the monoatomic metals. The  $\gamma(\text{Ni})/\gamma'(\text{Ni}_3\text{Al})$  supercell model contains 64 atoms and two interfaces. The non-addition  $\gamma(\text{Ni})/\gamma'(\text{Ni}_3\text{Al})$  supercell is referred to as Noadd. The Ni or Al atoms labeled with digits (1, 2, 3 and 4) in the model Noadd have different distances from the interfaces. The four Re-addition interface models are constructed by replacing the labeled atoms with Re, as shown in figure 3. The models with Ni labeled by the numbers 1, 2 and 3 and Al labeled by the number 4 are replaced by Re and are referred to as Ni(1), Ni(2), Ni(3) and Al(4), respectively. Furthermore, to obtain the site preference of Re in Ni<sub>3</sub>Al, the binding energies of the two models Ni<sub>24</sub>Al<sub>7</sub>Re and Ni<sub>23</sub>Al<sub>8</sub>Re, which represent a  $2 \times 2 \times 2$  Ni<sub>3</sub>Al supercell model with one Al and one Ni atom replaced by a Re atom, are included in the fitting.

**2.3.2. Property calculations and related results.** The lattice parameters and binding energies of the virtual structures can be viewed as the basic characteristics of the interaction between different elements. The parameters in the cross-potentials of Ni–Re and Al–Re are obtained by minimizing the weighted mean square deviation between the calculated and first-principles data. The profiles of the pair potentials are also selected to be non-oscillating. The Ni–Re and Al–Re cross-potentials are shown in figure 1(c). The lattice parameters and binding energies of the ordered structures calculated with both Vienna Ab-initio Simulation Package [41, 42] (VASP) and the present potential are listed in table 3. It can be seen from table 3 that the lattice constants of the ordered structures calculated with the present potential are in

**Table 3.** Properties used in the fitting of the cross interactions of Ni–Re and Al–Re obtained from VASP calculations and compared with the present potential.

Formula	Structure	Lattice constants (Å)		Binding energy (eV/atom)	
		First principles	Present EAM	First principles <sup>a</sup>	Present EAM
Ni <sub>3</sub> Re <sup>b</sup>	L1 <sub>2</sub>	3.62	3.62	−5.26	−5.54
Ni <sub>3</sub> Re <sup>c</sup>	D0 <sub>19</sub>	$a = 5.18$ $c/a = 0.80$	$a = 5.12$ $c/a = 0.82$	−5.35	−5.55
Ni <sub>3</sub> Re <sup>c</sup>	D0 <sub>22</sub>	$a = 3.57$ $c/a = 2.07$	$a = 3.66$ $c/a = 1.92$	−5.36	−5.57
NiRe <sup>b</sup>	B2	2.95	2.94	−5.93	−6.55
Re <sub>3</sub> Al <sup>b</sup>	L1 <sub>2</sub>	3.91	3.95	−6.65	−6.64
AlRe <sup>b</sup>	B2	3.09	3.11	−5.71	−5.25
Al <sub>3</sub> Re <sup>b</sup>	L1 <sub>2</sub>	3.90	4.07	−4.60	−4.34
Ni <sub>2</sub> ReAl <sup>b</sup>	L2 <sub>1</sub>	5.88	5.84	−5.16	−5.43
Ni <sub>24</sub> Al <sub>7</sub> Re <sup>b</sup>	Supercell $2 \times 2 \times 2$	3.57	3.57	−4.77	−4.76
Ni <sub>23</sub> Al <sub>8</sub> Re <sup>b</sup>	Supercell $2 \times 2 \times 2$	3.59	3.59 <sup>d</sup>	−4.72	−4.74

<sup>a</sup> Scaled to match experimental database.<sup>b</sup> Relaxed with respect to the lattice parameters.<sup>c</sup> Relaxed with respect to unit cell volume, shape and all internal atomic positions.<sup>d</sup> Not included in the fitting database, but listed for comparison.**Table 4.** Heat of formation of pure and Re-addition  $\gamma$ (Ni)/ $\gamma'$ (Ni<sub>3</sub>Al) interface models calculated with the present potentials and from VASP.

Model	The heat of formation (eV/atom)	
	VASP	Present EAM
Ni(1) <sup>a,b</sup>	−0.26	−0.27
Ni(2) <sup>a,b</sup>	−0.24	−0.25
Ni(3) <sup>a,b</sup>	−0.20	−0.23
Al(4) <sup>a,b</sup>	−0.20	−0.21
Noadd <sup>b</sup>	−0.24	−0.24

<sup>a</sup> Included in the fitting database.<sup>b</sup> Relaxed with respect to unit cell volume, shape and all internal atomic positions.

good agreement with the respective first-principles results. The binding energies of the ordered structures are in fair agreement with the VASP calculations, with a root-mean-square deviation of 5.4%.

The fitting data of the models Ni(1), Ni(2), Ni(3) and Al(4) are assigned higher weights in the fitting to give the interaction between Re and the  $\gamma$ (Ni)/ $\gamma'$ (Ni<sub>3</sub>Al) interface. For the pure and Re-addition  $\gamma$ (Ni)/ $\gamma'$ (Ni<sub>3</sub>Al) interface supercell models, the results of the heat of formation calculated with the present potential and VASP are list in table 4. The present potential gives the order of heat of formation: Ni(1)<Ni(2)<Noadd<Ni(3)<Al(4). For models Ni(1), Ni(2) and Ni(3), the order of heat of formation is independent of the binding energies of the pure elements, which is consistent with the VASP and other first-principles calculations [11].

**2.3.3. Annotation for the calculation of lattice parameters and binding energies.** The first-principles calculations were performed using the VASP. We used the GGA for the exchange

correlation functional. All calculations were carried out in a spin-restricted mode. For the VASP calculations, the cutoff energy of the atomic wave function was set to be 350 eV. The accuracy for electronic minimization was  $10^{-4}$  eV, and ionic relaxation was  $10^{-2}$  eV Å<sup>-1</sup>.

The discrepancy of the lattice constants and binding energy between first-principles calculations and the experiments is related to the approximation of the exchange and correlation potential used in the calculations. The lattice parameters of the different structures from the first-principles calculations were directly used in the fitting. Although the VASP calculations using the GGA often overestimate the lattice constants of transition metals, the discrepancy between the first-principles and the experimental value may be ignored. For instance, in the work of Sheng *et al* [43] the lattice constants calculated with VASP were multiplied by a factor of between 0.97 and 0.99 to match the experimental lattice constants of the transition metals Ni, Cu, Ag and Au. Furthermore, the binding energies from the first-principles calculations usually need to be scaled to match the experimental values. The heat of formation equation (12) can be used to scale the binding energy that can be used as the target value in the fitting. The scaled binding energies are given by solving the equation

$$H^{\text{FP}} = [E_b(n, m, l) - n \times E_b^{\text{EXP}}(\text{Ni}) - m \times E_b^{\text{EXP}}(\text{Al}) - l \times E_b^{\text{EXP}}(\text{Re})]/(n + m + l). \quad (13)$$

$H^{\text{FP}}$  is the heat of formation per atom calculated with first principles using equation (12).  $E_b^{\text{EXP}}(\text{Ni})$ ,  $E_b^{\text{EXP}}(\text{Al})$  and  $E_b^{\text{EXP}}(\text{Re})$  are the experimental binding energies per atom.  $E_b(n, m, l)$  is the scaled binding energy. Thus, the binding energies  $E_b(n, m, l)$  of the virtual compounds calculated with equation (13) can be used in the fitting. The results are listed in table 3 and labeled ‘First-principles’.

### 3. Results for the present potentials

#### 3.1. Lattice constants, elastic constants and cohesive energies of Ni, Al, Re and Ni<sub>3</sub>Al

The basic characteristics of the interatomic interaction can be determined by the parametrized energy function through fitting the basic physical properties of monoatomic metals and alloys. The lattice constants, elastic constants and cohesive energies are used in the determination of the parameters. The fitting results for these three properties of Ni, Al, Re and Ni<sub>3</sub>Al are listed in table 5. The results of the Voter–Chen potential [23] and the Mishin potential [24] are also included in the table for comparison. It can be seen from table 5 that the three properties of Ni, Al, Re and Ni<sub>3</sub>Al calculated with the corresponding potentials are in excellent agreement with the experimental data.

The mechanical properties of metals and alloys can be represented by the elastic constants in different modes of deformation. In the EAM, the elastic constants of fcc and hexagonal close-packed (hcp) structures are restricted by the relations  $C_{12} - C_{44} > 0$  and  $(3C_{12} - C_{11})/2 > C_{13} - C_{44} > 0$ , respectively. The elastic constants of Ni, Al and Re satisfy these conditions. A common expression for the elastic constants of EAM is [52]

$$C_{ijkl} = C_{ijkl}^{(1)} + C_{ijkl}^{(2)}. \quad (14)$$

Here,  $C_{ijkl}^{(1)}$  are the elastic constants induced by homogeneous deformation and  $C_{ijkl}^{(2)}$  are the inner elastic constants related to the lattice inner degrees of freedom. For fcc-Ni, Al and L1<sub>2</sub>-Ni<sub>3</sub>Al, the inner elastic constants are zero because of the centrosymmetry of their structures. The inner elastic constants should be calculated for the hcp structure [53, 54].

**Table 5.** Lattice properties included in the fitting of Ni, Al, Re and Ni<sub>3</sub>Al compared with experimental values and other potentials.

		Elastic constants (Mbar)						
		$a_0$ (Å)	$E_c$ (eV)	$C_{11}$	$C_{12}$	$C_{44}$	$C_{13}$	$C_{33}$
Ni	Experiment	3.52 <sup>a</sup>	4.45 <sup>b</sup>	2.47 <sup>c</sup>	1.47 <sup>c</sup>	1.25 <sup>c</sup>		
	Present EAM	3.52	4.44	2.37	1.50	1.27		
	Voter–Chen <sup>d</sup>	3.52	4.45	2.44	1.49	1.26		
	Mishin <sup>e</sup>	3.52	4.45	2.41	1.51	1.27		
Al	Experiment	4.05 <sup>a</sup>	3.36 <sup>f</sup>	1.14 <sup>c</sup>	0.619 <sup>c</sup>	0.316 <sup>c</sup>		
	Present EAM	4.05	3.36	1.14	0.618	0.315		
	Voter–Chen <sup>d</sup>	4.05	3.36	1.07	0.652	0.322		
	Mishin <sup>e</sup>	4.05	3.36	1.17	0.601	0.317		
Ni <sub>3</sub> Al	Experiment	3.567 <sup>g</sup>	4.57 <sup>h</sup>	2.30 <sup>d</sup>	1.50 <sup>d</sup>	1.31 <sup>d</sup>		
	Present EAM	3.567	4.65	2.42	1.49	1.30		
	Voter–Chen <sup>d</sup>	3.573	4.59	2.46	1.37	1.23		
	Mishin <sup>e</sup>	3.571	4.63	2.36	1.54	1.27		
Re	Experiment	2.76 <sup>i</sup> (1.62 <sup>k</sup> )	8.03 <sup>a</sup>	6.16 <sup>j</sup>	2.73 <sup>j</sup>	1.61 <sup>j</sup>	2.06 <sup>j</sup>	6.83 <sup>j</sup>
	Present EAM	2.76 (1.62 <sup>k</sup> )	8.03	5.75	2.66	1.65	2.10	6.83

<sup>a</sup> [44]. <sup>b</sup> [45]. <sup>c</sup> [46]. <sup>d</sup> [23]. <sup>e</sup> [24]. <sup>f</sup> [47]. <sup>g</sup> [48]. <sup>h</sup> [49]. <sup>i</sup> [50]. <sup>j</sup> [51]. <sup>k</sup>  $c/a$  ratio.

$C_{ijkl}^{(1)}$  of equation (14) can be written as

$$\begin{aligned}
 C_{ijkl}^{(1)} = \frac{1}{V_c} \sum_{v=1}^{\mu} \left\{ F''(\rho_v) \sum_m f'(r_m) \frac{r_{mi} r_{mj}}{r_m} \sum_m f'(r_m) \frac{r_{mk} r_{ml}}{r_m} \right. \\
 + F'(\rho_v) \sum_m \left[ f''(r_m) - \frac{f'(r_m)}{r_m} \right] \frac{r_{mi} r_{mj} r_{mk} r_{ml}}{r_m^2} \\
 \left. + \frac{1}{2} \sum_m \left[ \phi''(r_m) - \frac{\phi'(r_m)}{r_m} \right] \frac{r_{mi} r_{mj} r_{mk} r_{ml}}{r_m^2} \right\}, \quad (15)
 \end{aligned}$$

where  $V_c$  is the volume of the unit cell containing  $\mu$  atoms ( $\mu = 1$  for Ni and Al,  $\mu = 2$  for Re and  $\mu = 4$  for Ni<sub>3</sub>Al), and the sum of  $m$  refers to all of the atoms around the  $v$ th reference atom. The inner elastic constants (in Voigt notation) for the hcp structure are

$$-C_{11}^{(2)} = -C_{22}^{(2)} = C_{12}^{(2)} = -C_{66}^{(2)} = \frac{1}{V_c} \frac{\Omega_{x,xy}^2}{\theta_{xx}} \quad (16)$$

and

$$C_{13}^{(2)} = C_{33}^{(2)} = C_{44}^{(2)} = 0, \quad (17)$$

where

$$\begin{aligned}
 \Omega_{x,xy} = -2 \left\{ \sum_m \left[ F'(\rho_e) f''(r_m) + \frac{1}{2} \phi''(r_m) \right] \frac{r_{mx} r_{mx} r_{my}}{r_m^2} \right. \\
 \left. + \sum_m \left[ F'(\rho_e) f'(r_m) + \frac{1}{2} \phi'(r_m) \right] \left( 1 - \frac{r_{mx} r_{mx}}{r_m^2} \right) \frac{r_{my}}{r_m} \right\}, \quad (18)
 \end{aligned}$$

$$\theta_{xx} = 2 \left\{ \sum_n \left[ F'(\rho_e) f''(r_n) + \frac{1}{2} \phi''(r_n) \right] \frac{r_{nx} r_{nx}}{r_n^2} + \sum_n \left[ F'(\rho_e) f'(r_n) + \frac{1}{2} \phi'(r_n) \right] \left( 1 - \frac{r_{nx} r_{nx}}{r_n^2} \right) \frac{1}{r_n} \right\}. \quad (19)$$

In equations (18) and (19), one of the two atoms in the unit cell of the hcp structure is set as the reference atom. The sum of  $m$  includes all the atoms around the reference atom, while the sum of  $n$  refers to the atoms that do not belong to the sublattice of the reference atom. The value of  $(1/V_c)(\Omega_{x,xy}^2/\theta_{xx})$  in equation (16) for Re calculated with the present EAM potential is 0.34 Mbar. The inner elastic constants calculated with the present EAM potential account for 5.9%, 12.8% and 21.9% of the total elastic constants  $C_{11}$ ,  $C_{12}$  and  $C_{66} = (C_{11} - C_{12})/2$ , respectively. Thus, it is necessary to consider the inner elastic constants in the fitting of the potential of Re.

### 3.2. Equations of state and structure stabilities for Ni, Al and Re

The equation of state includes information of atomic interactions in a large range of atomic spacings. The equations of state of Rose *et al* [55] (Rose equation) of Ni, Al and Re are included in the fitting of the present potential. The equations of state are shown in figure 4. For Ni and Al, the equations of state calculated with the present EAM potential are in reasonable agreement with Rose equations.

The energies of the structure stability are useful in making sure that the ground state is maintained in the MD simulations. For structure  $A$  of a metal, the energy of the structure stability with respect to structure  $B$  is defined as  $\Delta E = E_B - E_A$ , where  $E_A$  and  $E_B$  are the energies per atom of the metal of the equilibrium structures  $A$  and  $B$ , respectively. For fcc-Ni, fcc-Al and hcp-Re, the energies of the structure stability compared with other structures, such as body centered cubic (bcc), simple cubic (sc) and diamond structures, were calculated with the present, Voter–Chen and Mishin potentials. The results are listed in table 6. It can be seen from table 6 that the energies of the structure stability calculated with the three potentials are lower than those from first-principles calculations for the fcc, bcc, hcp and sc structures, and higher for some of the diamond structures.

### 3.3. Vacancy formation and migration energies of Ni, Al, Re and binding energy of Re atom clusters in Ni

Point defects are introduced as vacancies by thermal vibration and substitutional solutes by alloying elements in superalloys. Point defects are important for the mechanical properties of superalloys. The diffusion of alloying elements in the  $\gamma$  phase is correlated with creep properties and rafting [57]. The motion of dislocation is controlled by the pinning effects of solutes and the climbing behavior is also associated with diffusion. The vacancy formation and the migration energies in Ni, Al and Re calculated with the present EAM potential and other potentials as well as the experimental data are summarized in table 7. It can be seen from table 7 that the vacancy formation energies of Ni, Al and Re calculated with the present potential are in good agreement with the experimental data. The migration energies of Ni and Al calculated with the present potential and the Voter–Chen potential are lower than the experimental data. The Mishin potential gives a good result for the migration energy. For hcp-Re, there are two types of vacancy migration, which correspond to the migration of a vacancy out of the basal plane ( $(0001)$  plane) and in the basal plane. The migration of a vacancy in the basal plane of hcp-Re is preferred over that out of the basal plane.

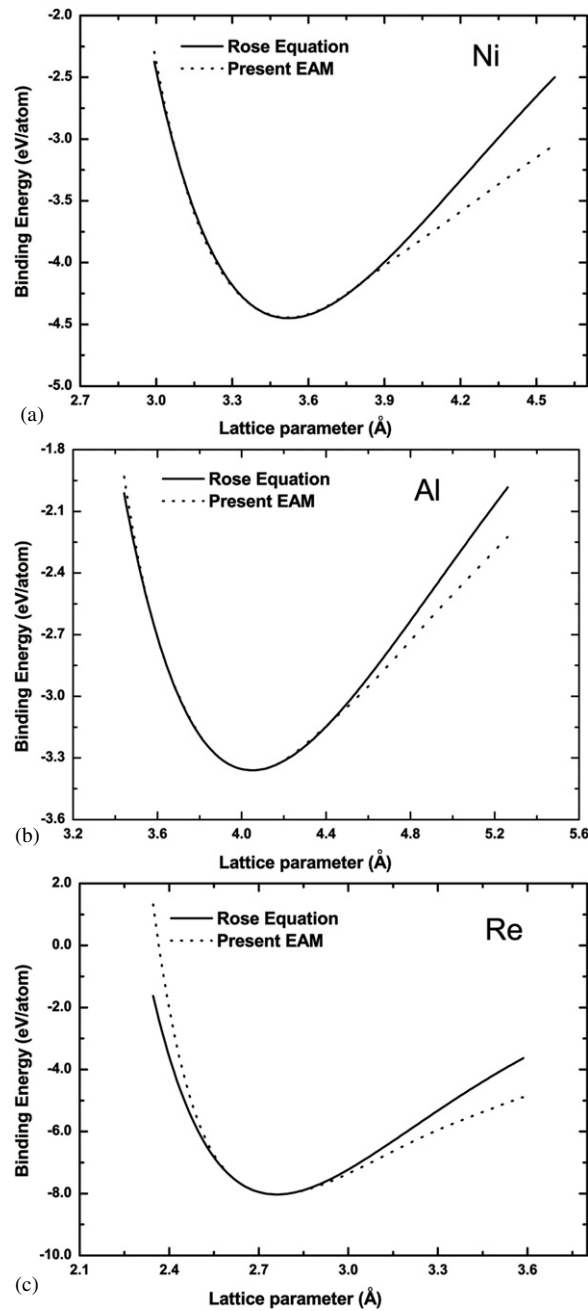


**Figure 4.** Equations of state for (a) Ni, (b) Al and (c) Re using the present EAM potential and the Rose equation.

Another test of the potential is whether the Re atoms form clusters in the  $\gamma$  phase, which is important to understand the mechanism of Re for the mechanical properties of the superalloy. The corresponding first-principles calculations have been performed in [8, 18]. The binding energy of  $n$  Re atoms is evaluated using a  $3 \times 3 \times 3$  supercell (108 atoms) and

**Table 6.** Energies (in eV/atom) of the structure stabilities for Ni, Al and Re.

Structure	fcc-Ni				fcc-Al				hcp-Re	
	LAPW <sup>a</sup>	Present EAM	Voter–Chen <sup>b,a</sup>	Mishin <sup>c</sup>	LAPW <sup>a</sup>	Present EAM	Voter–Chen <sup>b,a</sup>	Mishin <sup>c</sup>	VASP <sup>d</sup>	Present EAM
FCC									0.06	0.01
HCP	0.03	0.02	0.01	0.02	0.04	0.02	0.01	0.03		
BCC	0.11	0.07	0.10	0.07	0.09	0.06	0.07	0.09	0.32	0.13
SC	1.00	0.56	0.54	0.72	0.36	0.24	0.13	0.30	1.31	1.10
Diamond	1.94	1.04	1.84	1.42	0.75	0.58	0.84	0.88	1.49	1.65

<sup>a</sup> [56]. <sup>b</sup> [23]. <sup>c</sup> [24]. <sup>d</sup> Calculated in this work.

**Table 7.** Relaxed vacancy formation and migration energies for Ni, Al and Re.

	Ni				Al				Re	
	Experiment	Present EAM	Voter–Chen <sup>a</sup>	Mishin <sup>b</sup>	Experiment	Present EAM	Voter–Chen <sup>a</sup>	Mishin <sup>b</sup>	Experiment	Present EAM
$E_v^f$ (eV)	1.60 <sup>c</sup>	1.57 <sup>d</sup>	1.56	1.57	0.75 <sup>e</sup>	0.76 <sup>d</sup>	0.63	0.71	2.30 <sup>f</sup>	2.33 <sup>d</sup>
$E_v^m$ (eV)	1.30 <sup>c</sup>	0.98	0.98	1.19	0.65 <sup>g</sup>	0.48	0.30	0.65		2.47 <sup>h</sup> 2.62 <sup>i</sup>

<sup>a</sup> [23]. <sup>b</sup> [24]. <sup>c</sup> [58]. <sup>d</sup> Included in the fitting database. <sup>e</sup> [59]. <sup>f</sup> [60]. <sup>g</sup> [61]. <sup>h</sup> In the basal plane. <sup>i</sup> Out of the basal plane.

the following equation:

$$E_{\text{binding}}(n\text{Re}) = E(\text{Ni}_{108-n}\text{Re}_n) + (n - 1) \times E(\text{Ni}_{108}) - n \times E(\text{Ni}_{107}\text{Re}_1). \quad (20)$$

Here,  $E(\text{Ni}_{108})$ ,  $E(\text{Ni}_{107}\text{Re}_1)$  and  $E(\text{Ni}_{108-n}\text{Re}_n)$  are the energies of the pure Ni lattice, the Ni lattice containing one Re atom and the Ni lattice with  $n$  Re atoms placed at the first or second nearest neighboring (1NN or 2NN) sites (see figure 5), respectively. A positive binding energy indicates a repulsive interaction between  $n$  Re atoms and a negative one indicates an attractive interaction. It can be seen from figures 5(a) and (b) that the binding energies of 1NN and 2NN clusters calculated with the present potential and VASP increase with the increasing of the number of Re atoms. The binding energy of two Re 1NN cluster calculated with the present potential is 0.24 eV. Although the repulsive interaction of two Re 1NN cluster is less than that from first-principles calculations of 0.43 eV [8, 18], the result indicates that Re atoms do not tend to form 1NN clusters when considering the thermal vibration energy  $k_b T = 0.11$  eV ( $T = 1300$  K). The binding energies of 2NN clusters calculated with the present potential are in good agreement with those from VASP (see figure 5(b)). The binding energies of 2NN clusters calculated from both EAM and VASP are also energetically unfavorable in fcc-Ni. Thus, the Re atoms do not tend to form clusters in Ni. This result is consistent with the experiments of Mottura *et al* [7–9].

### 3.4. Concentration of vacancies and antisites in $\text{Ni}_3\text{Al}$ and site preference of Re in $\text{Ni}_3\text{Al}$

The  $\gamma'$  phase of  $\text{Ni}_3\text{Al}$  has  $\text{L1}_2$  crystalline structure. This compound, with the composition range 72.5–77 at% Ni at room temperature, is an important phase for strengthening the superalloys. Point defects, such as antisite defects, vacancies and interstitials, can be introduced by thermal motion and the deviation from stoichiometry; the latter is referred to as constitutional defects [63]. The properties of point defects, particularly vacancies and antisite defects, play an important role in diffusion in bulk materials. We calculated the equilibrium concentrations

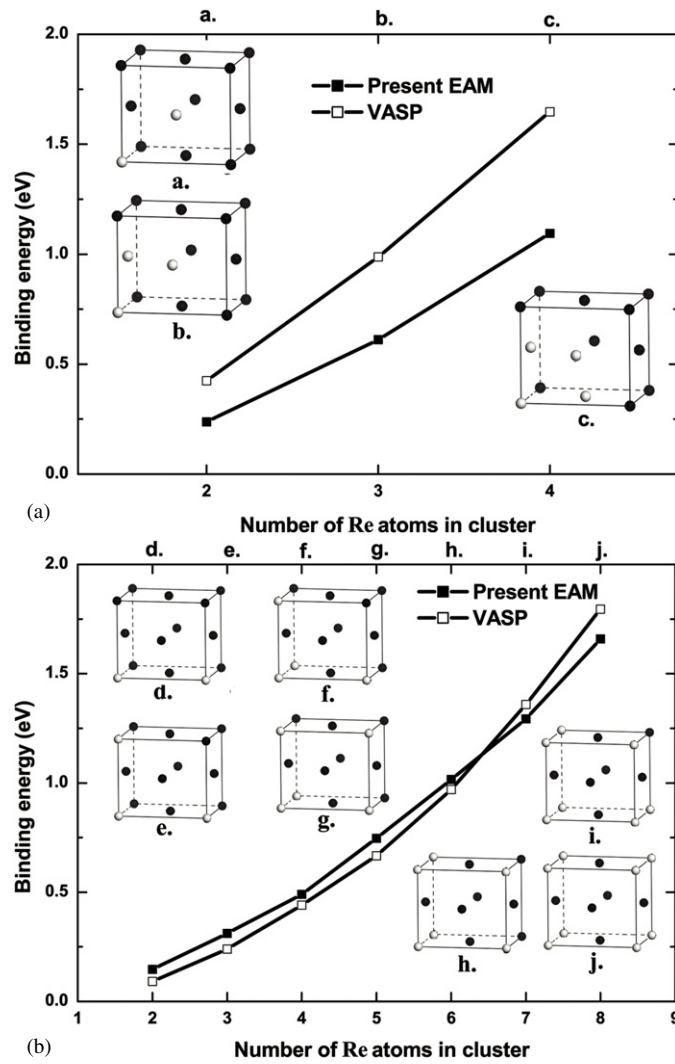


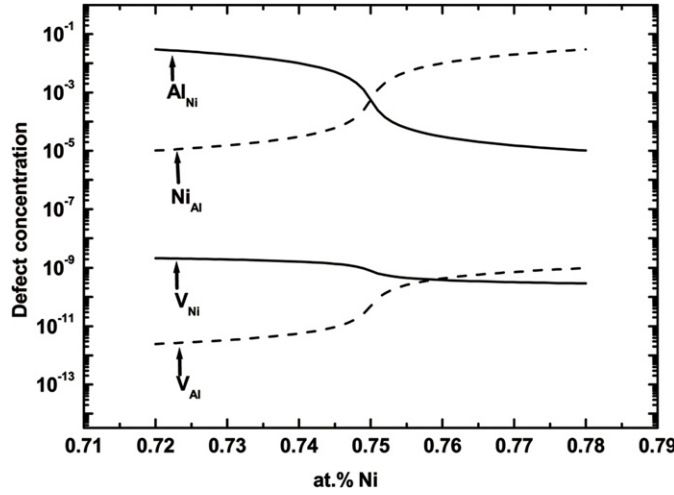
**Figure 5.** Binding energies of (a) 1NN and (b) 2NN Re clusters in a  $3 \times 3 \times 3$  fcc-Ni supercell. The atomic configurations of Re clusters (a.–j.) are shown in the insets. The black and white balls denote Ni and Re atoms, respectively. The data of VASP were directly extracted from figures in [18] using the software G3DATA [62]. Reprinted from [18] with permission from Elsevier.

of point defects in  $\text{Ni}_3\text{Al}$ , following the scheme proposed in [63]. Neglecting interstitials, there are four types of point defects: vacancies  $V_{\text{Ni}}$  and  $V_{\text{Al}}$ , and antisites  $\text{Ni}_{\text{Al}}$  and  $\text{Al}_{\text{Ni}}$  (the subscript refers to the sublattice). The concentrations of point defects can be calculated with the raw defect formation energy. The raw defect formation energy  $\epsilon_P = E(P) - E(0)$ , where  $E(P)$  and  $E(0)$  are the total energy of the system with defect  $P$  and that of the perfect system, respectively. The simulation system contained 864 atoms with the periodic boundary condition. The effects of atomic vibrations and thermal expansion were neglected. The raw formation energies of the four types of point defects are listed in table 8. Figure 6 shows the point defect concentrations as a function of composition at  $T = 1000$  K and  $p = 0$  ( $p$  is the external pressure). From figure 6, the antisites strongly dominate over vacancies in the



**Table 8.** Calculated raw formation energies of a point defect in Ni<sub>3</sub>Al.

	$\epsilon_P$ (eV)			
	V <sub>Ni</sub>	V <sub>Al</sub>	Ni <sub>Al</sub>	Al <sub>Ni</sub>
Ni <sub>3</sub> Al	6.40	6.67	0.66	0.49

**Figure 6.** Calculated concentrations of point defects in Ni<sub>3</sub>Al as a function of the composition of Ni at 1000 K.

appropriate composition region. In Ni-rich compositions, the excess Ni atoms reside on the Al sublattice sites as Ni<sub>Al</sub> antisites. Likewise, in Al-rich compositions the excess Al atoms reside on the Ni sublattice sites as Al<sub>Ni</sub> antisites. This is in agreement with the experimental work of Dasgupta *et al* [64].

The effective formation energies [24] of point defects in the compounds can be calculated from the slopes of the experimental Arrhenius plots of defect concentrations. It is useful to compare between theoretical calculation and experiments. The effective formation energies of point defects in compounds depend on the alloy composition. The concentrations of defects in Ni-rich, Al-rich and stoichiometric Ni<sub>3</sub>Al follow the Arrhenius relationship but with different exponents or effective formation energies. In stoichiometric Ni<sub>3</sub>Al, the Ni vacancy is dominant over the Al vacancy. The effective formation energy of Ni vacancies in stoichiometric Ni<sub>3</sub>Al is given by [24]

$$E_{V_{Ni}}^{\text{eff}} = \epsilon_{V_{Ni}} + E_0 + \frac{1}{8}(\epsilon_{Ni_{Al}} - \epsilon_{Al_{Ni}}), \quad (21)$$

where  $\epsilon_P$  is the raw defect formation energy of defect  $P$  and  $E_0$  is the energy per atom of the perfect Ni<sub>3</sub>Al system. The  $E_{V_{Ni}}^{\text{eff}}$  calculated with the present potential is 1.77 eV, which is in good agreement with the experimental value of  $1.6 \pm 0.2$  eV [65]. Ni is believed to diffuse along its own sublattice by a vacancy mechanism [66]. The jump barrier of a Ni vacancy in the Ni sublattice calculated with the present potential is 1.10 eV. The activation energy  $Q$  of Ni diffusion in stoichiometric Ni<sub>3</sub>Al is 2.87 eV, which is equal to the result of the Mishin potential of 2.87 eV [24].

The mechanical properties of Ni<sub>3</sub>Al can be improved by doping with alloying elements. The site preference is useful to understand the role of the alloying elements on the mechanical properties. According to Jiang and Gleeson [67], the parameter  $E_{\text{Re}}^{\text{Ni} \rightarrow \text{Al}}$  can describe the site

**Table 9.** Planar fault energies (in  $\text{mJ m}^{-2}$ ) of Ni and Al calculated with the present EAM potential, other potentials and the experimental values. The experimental surface energies are for the average orientation.

Property	Ni				Al			
	Experiment	Present EAM	Voter–Chen <sup>a</sup>	Mishin <sup>b</sup>	Experiment	Present EAM	Voter–Chen <sup>a</sup>	Mishin <sup>b</sup>
Stacking faults								
$\gamma_{\text{sf}}$	125 <sup>c</sup>	102 <sup>d</sup>	58	134	166 <sup>c</sup>	82 <sup>d</sup>	76	115
$\gamma_{\text{us}}$		282	225	298		139	93	151
Surfaces								
(1 0 0)	2280 <sup>c</sup>	1591	1745	1936	980 <sup>c</sup>	694	855	607
(1 1 0)	2280 <sup>c</sup>	1694	1977	2087	980 <sup>c</sup>	751	959	792
(1 1 1)	2280 <sup>c</sup>	1499	1621	1759	980 <sup>c</sup>	658	823	601

<sup>a</sup> [23]. <sup>b</sup> [24]. <sup>c</sup> [69]. <sup>d</sup> Included in the fitting database.

preference behavior of Re in  $\text{Ni}_3\text{Al}$  at  $T = 0$  K, and is given by

$$E_{\text{Re}}^{\text{Ni} \rightarrow \text{Al}} = E(\text{Ni}_{24}\text{Al}_7\text{Re}) - E(\text{Ni}_{23}\text{Al}_8\text{Re}) + E(\text{Ni}_{23}\text{Al}_8\text{Al}) - E(\text{Ni}_{24}\text{Al}_8), \quad (22)$$

where  $E(\text{Ni}_{24}\text{Al}_7\text{Re})$ ,  $E(\text{Ni}_{23}\text{Al}_8\text{Re})$  and  $E(\text{Ni}_{24}\text{Al}_8)$  are the binding energies of the models  $\text{Ni}_{24}\text{Al}_7\text{Re}$ ,  $\text{Ni}_{23}\text{Al}_8\text{Re}$  (see section 2.3.1) and a  $2 \times 2 \times 2$   $\text{Ni}_3\text{Al}$  supercell, respectively.  $E(\text{Ni}_{23}\text{Al}_8\text{Al})$  is the binding energy of a  $2 \times 2 \times 2$   $\text{Ni}_3\text{Al}$  supercell with one Ni replaced by Al.  $E_{\text{Re}}^{\text{Ni} \rightarrow \text{Al}}$  represents the energy required to transfer one Re atom from a Ni sublattice to an Al sublattice.  $E_{\text{Re}}^{\text{Ni} \rightarrow \text{Al}}$  calculated with the present potential is  $-0.16$  eV. According to Jiang, this indicates that Re has a preference for the Al sublattice sites in Al-rich, Ni-rich and stoichiometric  $\text{Ni}_3\text{Al}$ , which is qualitatively consistent with the first-principles results [67].

### 3.5. Stacking fault and surface energies of Ni, Al and Re

Planar faults play an important role in the mechanical properties of materials. The glide and climb of dislocations are affected by stacking faults in crystalline crystals. The lower stacking fault energy of the Ni solid solution can decrease the steady-state creep rate of the  $\gamma$  phase [68]. The brittle/ductile fracture is a competition between forming surfaces and creating dislocations from the crack tip.

The stacking fault energy ( $\gamma_{\text{sf}}$ ) and the unstable stacking energy ( $\gamma_{\text{us}}$ ) calculated with the present, Voter–Chen and Mishin potentials are compared with the experimental values and listed in table 9. The stacking fault energy of Ni calculated with the present potential is in reasonable agreement with the experimental value, but less accurate for Al. The stacking fault energies of Ni calculated with the Cai–Ye potential and the present Ni potential are  $6 \text{ mJ m}^{-2}$  and  $102 \text{ mJ m}^{-2}$ , respectively. For the present Ni potential, the contribution of the pair potential to the stacking fault energy is  $99 \text{ mJ m}^{-2}$ . Thus, the effect of the modification to the Cai–Ye potential is obvious for this property. The surface energies of the low-index faces of Ni and Al using the present, Voter–Chen and Mishin potentials are consistently underestimated compared with the experimental data (see table 9). For Ni and Al, the close-packed (1 1 1) face has the lowest energy, followed by the (1 0 0) and (1 1 0) faces. This trend is in agreement with other studies [26]. The surface energy of Ni calculated with the present potential on the (1 1 1) surface is less than that with the Voter–Chen and the Mishin potentials. However, the brittle/ductile behavior of Ni depends on the ratio  $\gamma/\gamma_{\text{us}}$ , where  $\gamma$  and  $\gamma_{\text{us}}$  are the surface energy of the (1 1 1) surface and the unstable stacking energy, respectively. Rice [70] pointed out that the fcc metal under ‘Mode I’ loading is intrinsically ductile if  $D = 0.3(\gamma/\gamma_{\text{us}}) > 1$ .

**Table 10.** Planar faults energies (in  $\text{mJ m}^{-2}$ ) of Re calculated with the present EAM potential compared with experiments and the tight-binding method. The experimental surface energies are for the average orientation.

Property	Re	
	Experiment or tight binding	Present EAM
Stacking faults		
$I_2$	540 <sup>a</sup>	60 <sup>b</sup>
$I_1$		31
Surfaces		
Basal plane (000 1)	3600 <sup>c</sup> , 3630 <sup>d</sup>	1544
Prism plane (11 $\bar{2}$ 0)		1851

<sup>a</sup> [71]. <sup>b</sup> Included in the fitting database. <sup>c</sup> [72]. <sup>d</sup> [73].**Table 11.** Planar fault energies (in  $\text{mJ m}^{-2}$ ) of  $\text{Ni}_3\text{Al}$  calculated with the present potential compared with other potentials and experiments. The contributions of the embedding energy term and the pair potential term are also listed; Total = Embed + Pair.

Planar Fault	(111)CSF			(111)APB			(111)SISF			(100)APB		
	Total	Pair	Embed	Total	Pair	Embed	Total	Pair	Embed	Total	Pair	Embed
Experiment <sup>a</sup>	235			175			6			104		
Present EAM	218 <sup>b</sup>	301	−83	168 <sup>b</sup>	274	−106	14 <sup>b</sup>	−43	57	102 <sup>b</sup>	65	37
Voter–Chen <sup>c</sup>	120	119	1	141	140	1	12	6	6	83	80	3
Mishin <sup>d</sup>	202	217	−15	252	267	−15	51	42	9	80	53	27

<sup>a</sup> [75]. <sup>b</sup> Included in the fitting database. <sup>c</sup> [23]. <sup>d</sup> [24].

The  $D$  values calculated with the present, Voter–Chen and Mishin potentials are 1.60, 2.16 and 1.77, respectively, which are consistent with the intrinsic ductility of Ni. Therefore, the present potential correctly predicts the basic mechanical behavior of Ni.

The  $I_2$  (ABABCACA stacking) and  $I_1$  (ABABCBCB stacking) stacking fault energies of hcp-Re on the basal plane are shown in table 10. The energy of the intrinsic fault  $I_2$  is much lower than that reported by Legrand [71] using a tight-binding method. The quantum effect in the stacking fault of Re is too strong and the EAM cannot give a reasonable fit. The energy for the intrinsic fault  $I_1$  is half of the  $I_2$  fault, which is consistent with the relation given by Hull and Bacon [74]. The calculated surface energies (see table 10) for the basal and prism planes are less than the corresponding experimental values.

### 3.6. Planar defect energies of $\text{Ni}_3\text{Al}$ and the effect of the many-body term on the planar defect energies

In  $\gamma/\gamma'$  superalloys, the planar fault of the APB is an important barrier for dislocation crossing the ordered  $\gamma'$  phase [57]. The yield stress anomaly of  $\text{Ni}_3\text{Al}$  is also related to the APB energy anisotropy. The planar faults of  $\text{Ni}_3\text{Al}$  fitted in the present potential include the CSF on the (111) plane, the superlattice intrinsic stacking fault (SISF) on the (111) plane, and the APB fault on the (111) and (100) planes. The planar fault energies of  $\text{Ni}_3\text{Al}$  calculated with the present potential, the Voter–Chen and the Mishin potentials are listed in table 11. From table 11, there is good agreement between the experimental values and the four types of planar fault energies calculated with the present potential. In particular, the (111) CSF energy calculated with the present potential is larger than the (111) APB energy, which is in

agreement with the experimental value and the results of first-principles calculations [76, 77]. The (1 1 1) CSF and (1 1 1) APB energies involve the chemical bond change from a Ni–Al bond to a Al–Al bond. This energy contribution from the change of the chemical bond to the planar fault energies can be given by the embedding energy term and the effective pair potential term in the EAM. To understand the difference between the present Ni–Al potential and the Voter–Chen and the Mishin potentials, the contributions of the embedding energy and effective pair potential terms to the planar fault energy are calculated, and are also listed in table 11. It can be seen from table 11 that the contributions of the embedding energy of the Voter–Chen and Mishin potentials to the four planar fault energies are much smaller than those of the present potential. This indicates that both the embedding energy and the pair potential have important influences on the planar fault energies in the present EAM potential, while the planar fault energies calculated with the Voter–Chen and Mishin potentials are mainly due to the effective pair potentials. The embedding energy is a function of host electron density, and the host electron density is the superposition of atomic electron densities. Hence, the difference between the present and the other two potentials originates from the atomic electron density. The host electron densities of Ni and Al at the equilibrium lattice structure of Ni<sub>3</sub>Al are  $\rho_{\text{Ni}}/\rho_{\text{e}}^{\text{Ni}} = 2.3$  and  $\rho_{\text{Al}}/\rho_{\text{e}}^{\text{Al}} = 0.5$  for the present potential,  $\rho_{\text{Ni}}/\rho_{\text{e}}^{\text{Ni}} = 1.1$  and  $\rho_{\text{Al}}/\rho_{\text{e}}^{\text{Al}} = 1.2$  for the Voter–Chen potential, and  $\rho_{\text{Ni}}/\rho_{\text{e}}^{\text{Ni}} = 1.0$  and  $\rho_{\text{Al}}/\rho_{\text{e}}^{\text{Al}} = 1.2$  for the Mishin potential. The embedding energies have minimum values at  $\rho/\rho_{\text{e}} = 1$  (see figure 1(b)). The force on atom is correlated with the first derivative of embedding energy  $F'(\rho)$ . The absolute value of  $F'(\rho)$  decreases with decreasing  $|\rho - \rho_{\text{e}}|$ . The host electron densities  $\rho_{\text{Ni}}$  and  $\rho_{\text{Al}}$  of the Voter–Chen and Mishin potentials in Ni<sub>3</sub>Al are much closer to  $\rho_{\text{e}}^{\text{Ni}}$  and  $\rho_{\text{e}}^{\text{Al}}$  than those of the present potential. Thus, the embedding energy terms of the Voter–Chen and Mishin potentials only have a minor effect in Ni<sub>3</sub>Al compared with the present potential. This indicates that the effect of the many-body term or embedding energy term on the properties of alloys should be considered when constructing the alloy potentials. The host electron density of the Ni and Al atoms in the equilibrium lattice structure of Ni<sub>3</sub>Al is affected by the parameter  $s_{\text{Al}}$  in the three potentials. Hence, the parameters of the potential related to the atomic electron density should be considered in the numerical fitting of the potential parameters.

### 3.7. Effect of Re on the interface lattice misfit between $\gamma(\text{Ni})$ and $\gamma'(\text{Ni}_3\text{Al})$

The  $\gamma/\gamma'$  interface lattice misfit of superalloys, which is correlated with the elevated temperature mechanical properties, is affected by the partitioning of the alloying elements between the  $\gamma$  and  $\gamma'$  phases [78, 79]. More fine  $\gamma/\gamma'$  interfacial dislocation network and more negative lattice misfit are the important strengthening factors of superalloys [80, 81]. Thus, the influence of Re on the interface lattice misfit of the superalloys should be considered. A  $2 \times 2 \times 2$  supercell of fcc-Ni is used to represent the  $\gamma(\text{Ni})$  phase, and the Re-doped  $\gamma(\text{Ni}(\text{Re}))$  phase is constructed by replacing a Ni atom of the supercell with Re. Similarly, the Re-doped  $\gamma'(\text{Ni}_3(\text{Al}, \text{Re}))$  phase is constructed by replacing an Al atom of a  $2 \times 2 \times 2$  supercell of  $\gamma'(\text{Ni}_3\text{Al})$  with Re. The lattice misfit is defined as

$$\delta = 2 \frac{a_{\gamma'} - a_{\gamma}}{a_{\gamma'} + a_{\gamma}}, \quad (23)$$

where  $a_{\gamma}$  and  $a_{\gamma'}$  are the lattice parameters of the  $\gamma$  and  $\gamma'$  phases, respectively. The lattice parameters of the models were obtained by minimizing the total energies of the supercells with respect to the local atomic displacements and the supercell volume. The results of the lattice parameters and misfits calculated with the present potential are listed in table 12 and compared with the results from first-principles calculations [82]. It can be seen from table 12 that Re increases the lattice parameters of both  $\gamma(\text{Ni})$  and  $\gamma'(\text{Ni}_3\text{Al})$ . By adding the same Re

**Table 12.** Calculated lattice parameters and lattice misfits of  $\gamma(\text{Ni})$ ,  $\gamma'(\text{Ni}_3\text{Al})$ , alloyed  $\gamma(\text{Ni}(\text{Re}))$ , and  $\gamma'(\text{Ni}_3(\text{Al},\text{Re}))$  with the present potential and from first-principles calculations.

	VASP <sup>a</sup>		Present EAM	
	$a$ (Å)	$\delta$ (%)	$a$ (Å)	$\delta$ (%)
$\gamma(\text{Ni})$	3.515	1.50	3.520	1.33
$\gamma'(\text{Ni}_3\text{Al})$	3.568		3.567	
$\gamma(\text{Ni}(\text{Re}))$	3.526	1.32	3.531	1.10
$\gamma'(\text{Ni}_3(\text{Al},\text{Re}))$	3.573		3.570	

<sup>a</sup> [82].

concentration (3.1 at%) to  $\gamma(\text{Ni})$  and  $\gamma'(\text{Ni}_3\text{Al})$ , the increase in the lattice parameter of  $\gamma(\text{Ni})$  is larger than that for  $\gamma'(\text{Ni}_3\text{Al})$ , which leads to the lattice misfit decreasing. The results from the present potential are consistent with first-principles calculations [82].

### 3.8. Interaction between Re and the misfit dislocation on the $\gamma(\text{Ni})/\gamma'(\text{Ni}_3\text{Al})$ interface

The  $\gamma/\gamma'$  superalloys have good creep resistance, which is related to the  $\gamma/\gamma'$  interfaces retarding the dislocation motion [83]. The pinning effect of solute on a misfit dislocation is associated with the interaction between the solute and the dislocation. The concentration of Re near the  $\gamma/\gamma'$  interface is small, about 3 at%. The Re atoms do not tend to form clusters, as shown in section 3.3. Hence, the single impurity model is used to investigate the interaction between Re and the misfit dislocation on the  $\gamma(\text{Ni})/\gamma'(\text{Ni}_3\text{Al})$  interface. A  $\gamma(\text{Ni})/\gamma'(\text{Ni}_3\text{Al})$  interface model with the (001) interface oriented along the axes  $x = [110]$ ,  $y = [\bar{1}10]$ , and  $z = [001]$  (see figure 7(a)) was constructed [13]. The lower part is  $\gamma(\text{Ni})$ , with box vectors  $(n + 0.5)[110]$ ,  $(n + 0.5)[\bar{1}10]$  and  $15[001]$ , and the upper part is  $\gamma'(\text{Ni}_3\text{Al})$  with box vectors  $n[110]$ ,  $n[\bar{1}10]$  and  $15[001]$ , where  $n = 37$  is calculated from the relationship  $(n + \frac{1}{2})a_\gamma\sqrt{2} = na_{\gamma'}\sqrt{2}$ ,  $a_\gamma$  (3.52 Å) and  $a_{\gamma'}$  (3.567 Å) are the lattice parameters of  $\gamma(\text{Ni})$  and  $\gamma'(\text{Ni}_3\text{Al})$ , respectively. The model is periodic along the  $x$  and  $y$  directions and has free surfaces on the upper and lower bounds in the  $z$  direction. The glide plane or interface is defined to be in the middle between  $\gamma(\text{Ni})$  and  $\gamma'(\text{Ni}_3\text{Al})$ . The model contains 333 030 atoms. The energy of the atoms near the interface is not affected by the surfaces. The influence of the surface on the energy of atom is within a distance from the surfaces of about  $3a_0$ . There are two types of stacking sequences for the (001) interface. The atomic structure of  $\gamma(\text{Ni})$  can be constructed by stacking (001) planes of A and B, as shown in figure 7(b). Similarly, the atomic structure of  $\gamma'(\text{Ni}_3\text{Al})$  can be constructed by stacking (001) planes of A' and B'. The plane B' is identical with plane B. Provided there are no two layers of the same letter index, such as A'A and B'B, stacked together, the stacking sequence of the (001) interface can be type (a)  $\cdots A'B'A'B'|ABAB\cdots$  or type (b)  $\cdots B'A'B'A'|BABA\cdots$ , where the vertical bar denotes the glide plane or the interface. The energies of systems were minimized using the present EAM potential with a time step of  $5 \times 10^{-15}$  s and lattice misfit dislocations were formed on the interfaces, as shown in figure 7(a). The atomic structures of misfit dislocations on the two types of interfaces are also different. The atomic structures of the dislocations are visualized by the common neighbor analysis [84] (CNA) and presented in figure 7. The Burgers vectors of the dislocations are found to be of the  $\frac{1}{2}\langle 110 \rangle$  type, which is consistent with the experimental observation [85, 86]. To investigate the interaction between Re and the dislocation on the interface, we let a Re atom interact with a dislocation line far away from the intersection of the two dislocations. In the two interface models with the above stacking sequences (a) and (b), the Ni or Al atoms in different (001) planes are substituted by a Re

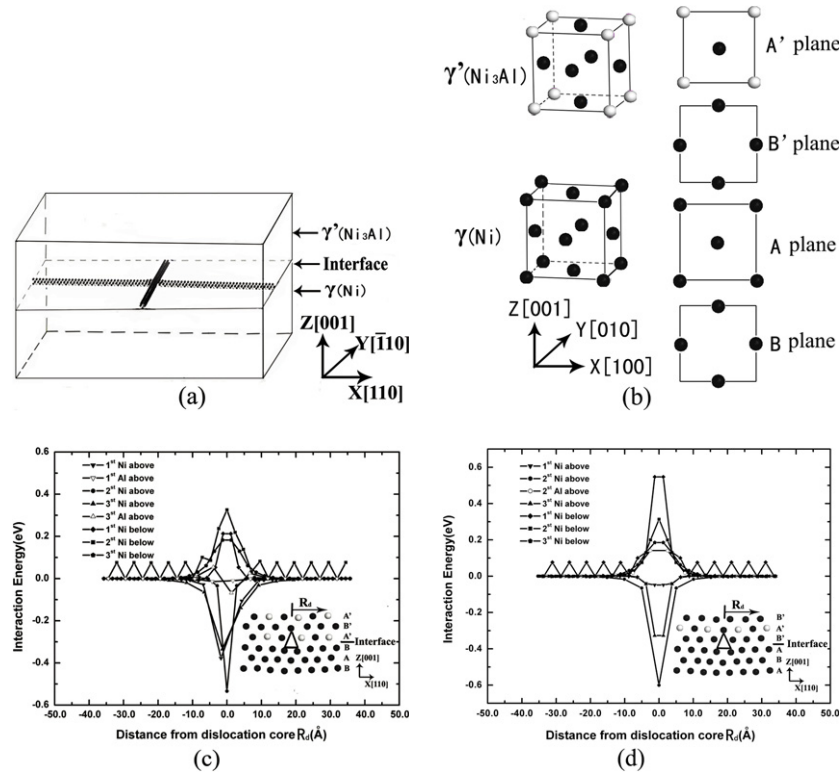


**Figure 7.** Relaxed  $\gamma(\text{Ni})/\gamma'(\text{Ni}_3\text{Al})$  lattice misfit interface model and the interaction energy between Re and the misfit dislocation. The lattice misfit dislocations on the  $\gamma(\text{Ni})/\gamma'(\text{Ni}_3\text{Al})$  interface are shown by the common neighbor analysis. The black and white balls denote Ni and Al atoms, respectively. The triangle in the inset figures denotes the dislocation core. (a) Relaxed lattice misfit dislocation on the  $\gamma(\text{Ni})/\gamma'(\text{Ni}_3\text{Al})$  interface. (b) Atomic configurations and the stacking sequence of  $\gamma(\text{Ni})$  and  $\gamma'(\text{Ni}_3\text{Al})$ . (c) Interaction energy between Re and the misfit dislocation with the stacking sequence of  $(\cdots B'A'B'A' | BABA \cdots)$ . (d) Interaction energy between Re and the misfit dislocation with the stacking sequence of  $(\cdots A'B'A'B' | ABAB \cdots)$ .

atom. The present EAM potential was then used to minimize the energy of the system. The Re-dislocation interaction energy ( $E_I$ ) is defined as a function of the distance ( $R_d$ ) from the dislocation core in the  $n$ th (001) plane,  $E_I(R_d, n) = E(R_d, n) - E(\infty, n)$ , where  $E(R_d, n)$  and  $E(\infty, n)$  are the total energies of the systems with a Re atom located at  $R_d$  in the  $n$ th (001) plane and  $R_d = \infty$ , respectively.  $E_I$  was plotted as a function of distance from the dislocation core along the  $[110]$  direction, and is shown in figures 7(c) and (d). The atomic structures of the misfit dislocation cores are shown in the insets. The plots in figures 7(c) and (d) show the repulsion on the side of Ni and the attraction on the side of  $\text{Ni}_3\text{Al}$ . The most negative interaction energies in the two stacking sequence types (a) and (b) are  $-0.53$  eV and  $-0.60$  eV, respectively, where the Ni atom in the second (001) plane above the glide plane is substituted by Re. Hence, the pinning effect of Re on the misfit dislocation is effective.

#### 4. Discussion

The effect of embedding energy on the planar fault energies ((111)APB, (100)APB, (111)CSF and (111)SISF) of  $\text{Ni}_3\text{Al}$  was analyzed. Different from the previous Ni–Al

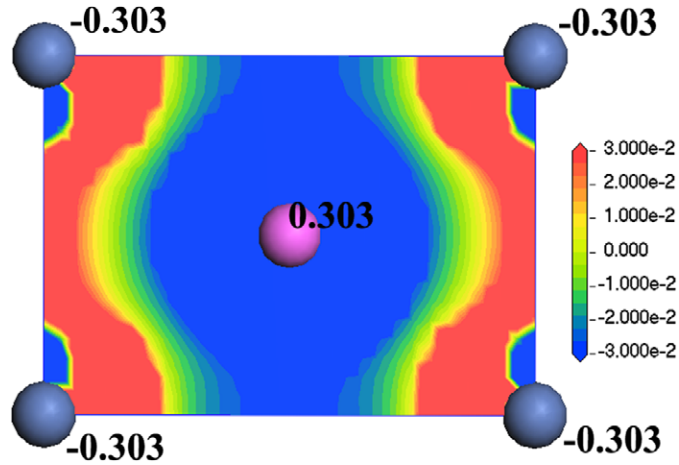


**Figure 8.** Electron density difference of the (1 1 0) plane of B2-NiAl. The blue and pink balls denote Ni and Al atoms, respectively. The charge partitioning between Ni and Al given by the Hirshfeld method is shown on the atoms.

potentials, the embedding energy term has an important effect on the four planar fault energies. This difference originates from the determination of parameter  $s_{Al}$ . The parameter  $s_{Al}$  is related to the elastic constants difference  $C_{12} - C_{44}$  of  $Ni_3Al$ . However, two values of  $s_{Al}$  can be given by the elastic constants' relationship. Then the host electron density of EAM is related to the charge partitioning between Ni and Al calculated from first principles. The element with increased actual electron density has a higher host electron density compared with its equilibrium host electron density  $\rho_e$  in the monoatomic metal. According to this criterion, one of the two  $s_{Al}$  values can be selected. It is interesting to examine whether the relationship between the charge partitioning and host electron density is correct in B2-NiAl. The present potential is constructed for the  $L1_2$ - $Ni_3Al$  system, and the B2-NiAl system is not completely considered. The lattice constant and cohesive energy of B2-NiAl calculated with the present potential are 2.83 Å and 4.52 eV, respectively, which are in good agreement with the experimental values, 2.88 Å [44] and 4.50 eV [49]. The equilibrium host electron densities of Ni and Al in B2-NiAl are  $\rho_{Ni}/\rho_e^{Ni} = 4.2$  and  $\rho_{Al}/\rho_e^{Al} = 0.92$ , which also correspond to the charge transfer from Al to Ni. The electron density difference of B2-NiAl on the (1 1 0) plane and the charge partitioning between Ni and Al calculated with Dmol3 are shown in figure 8. From figure 8, the trend of the charge transfer from Al to Ni is the same as the case of  $L1_2$ - $Ni_3Al$ . The host electron densities of the present potential for B2-NiAl are in agreement with the charge transfer calculated from first principles.  $C_{12} - C_{44}$  of B2-NiAl is also related to the parameter  $s_{Al}$ , just as in the case of  $L1_2$ - $Ni_3Al$ . The results of  $C_{12} - C_{44}$  for B2-NiAl calculated with the present potential and the corresponding experimental values are 0.22 Mbar ( $C_{12} = 2.23$  Mbar,  $C_{44} = 2.01$  Mbar) and 0.21 Mbar ( $C_{12} = 1.37$  Mbar,  $C_{44} = 1.16$  Mbar [87]), respectively. The  $C_{12} - C_{44}$  calculated with the present potential is also in agreement with that from experiment. It should be noted that the difference between the EAM and experimental value for the individual elastic constants of B2-NiAl can be improved by the pair potentials [25]. But the result of  $C_{12} - C_{44}$  is only related to the embedding energy and the pair potential cannot change the result. This result suggested that the parameters of potentials related to atomic electron density should be specially considered in the numerical fitting of the potentials based on the charge transfer between the elements. Although the physical properties calculated with EAM potential are controlled by both the embedding energy and pair potential, the effect of



embedding energy may be underestimated in the numerical fitting, such as the planar fault energies of  $\text{Ni}_3\text{Al}$ . Some special fitting strategies are needed to reveal the effect of embedding energy. The mechanical properties associated with planar fault can also be influenced by the special fitting strategies. One of the interesting features of  $\text{Ni}_3\text{Al}$  is the yield stress anomaly, which is due to two factors: the elastic anisotropy, and APB energy anisotropy [88–90]. The elastic anisotropy and APB energy anisotropy cause a driving force (or a torque force) that rotates the superdislocations on the (1 1 1) plane toward the cube (1 0 0) cross-slip plane [91]. The cross-slip of a segment of the superdislocations activated by thermal vibration forms locked configurations, which retard the motion of the dislocation. With increasing temperature, more locked superdislocations are formed and the yield stress increases. The driving force  $F_c$  (force per unit length of dislocation) for cross-slip due to the above two factors can be estimated by the expression

$$F_c = \gamma_{111} \frac{\sqrt{3}A}{A+2} - \gamma_{100}, \quad (24)$$

where  $\gamma_{100}$  and  $\gamma_{111}$  are the APB energies in the respective planes,  $A$  is Zener's anisotropy coefficient [92]  $A = 2C_{44}/(C_{11} - C_{12})$ . The larger the driving force  $F_c$ , the easier it is for cross-slip to occur. The values of  $F_c$  calculated with the present, Voter–Chen and Mishin potentials are  $67.6 \text{ mJ m}^{-2}$ ,  $46.5 \text{ mJ m}^{-2}$  and  $185.2 \text{ mJ m}^{-2}$ , respectively. The values of  $F_c$  calculated with experimental APB energies and elastic constants are  $71.8 \text{ mJ m}^{-2}$  and  $34.73 \text{ mJ m}^{-2}$  for 24 at% and 26 at% Al concentrations, respectively [93]. The  $F_c$  values calculated with the present potential and the Voter–Chen potential are in reasonable agreement with that from the experimental data. The Mishin potential overestimates the driving force, and first-principles calculations also show a similar trend [93]. The Mishin potential includes first-principles data in the fitting, which explains the higher  $F_c$  given by this potential. The values of  $\sqrt{3}A/(A+2)$  are 0.99 and 1.01 for the present and Mishin potentials, respectively. The driving force  $F_c$  is mainly determined by the difference between the (1 1 1) APB energy and the (1 0 0) APB energy. It can be seen from table 11 that the energy differences between (1 1 1) and (1 0 0) APB contributed by the pair potentials are  $214 \text{ mJ m}^{-2}$  and  $209 \text{ mJ m}^{-2}$  for the Mishin and present potentials, respectively. The energy differences between (1 1 1) and (1 0 0) APB contributed by the embedding energies are  $-42 \text{ mJ m}^{-2}$  and  $-143 \text{ mJ m}^{-2}$  for the Mishin and present potentials, respectively. Thus, the different cross-slip driving forces given by the Mishin and present potentials are mainly due to the contribution of the embedding energy. The embedding energy of the present potential has an important influence on the cross-slip driving force than that of the Mishin potential.

The structure stability of  $\gamma'(\text{Ni}_3\text{Al})$  is important for the MD simulation of superalloys. The binding energies of several alternate structures of  $\text{Ni}_3\text{Al}$  and  $\text{NiAl}$  were calculated with the present, Voter–Chen and Mishin potentials. The results are listed in table 13. For  $\text{Ni}_3\text{Al}$ , the  $\text{L}_{12}$  structure is most stable compared with the  $\text{D}_{023}$ ,  $\text{D}_{022}$ ,  $\text{D}_{03}$  and  $\text{D}_{019}$  structures for the Voter–Chen and Mishin potentials. The  $\text{L}_{12}\text{-Ni}_3\text{Al}$  is more stable compared with the  $\text{D}_{023}$ ,  $\text{D}_{022}$  and  $\text{D}_{03}$  structures for the present potential, except for the  $\text{D}_{019}$  structure. To test the stability of  $\text{L}_{12}\text{-Ni}_3\text{Al}$  in MD simulation, a simulation is carried out at a temperature of 1400 K, which is the operating temperature of the superalloys. The model contains 32 000 atoms, and the shape and volume of the model are adjusted to keep zero pressure in the simulation. The result shows that the  $\text{L}_{12}\text{-Ni}_3\text{Al}$  does not decompose into other structures. For  $\text{NiAl}$ , the  $\text{B}_2$  structure is the most stable compared with the  $\text{L}_{10}$ ,  $\text{B}_{32}$ ,  $\text{B}_{20}$ ,  $\text{L}_{11}$  and  $\text{B}_1$  structures for the three potentials. The energies along two uniform deformation paths [28] are calculated with the present, Voter–Chen and Mishin potentials. The first deformation path is that the  $\text{B}_2$  lattice



**Table 13.** Binding energies (eV/atom) of alternate structures of Ni<sub>3</sub>Al and NiAl calculated with the present, Voter–Chen and Mishin potentials.

Structure	Present EAM	Voter–Chen <sup>a</sup>	Mishin <sup>b</sup>
Ni <sub>3</sub> Al:			
L1 <sub>2</sub>	−4.65	−4.59	−4.63
D0 <sub>23</sub>	−4.64	−4.58	−4.62
D0 <sub>19</sub>	−4.65	−4.59	−4.62
D0 <sub>3</sub>	−4.60	−4.53	−4.61
D0 <sub>22</sub>	−4.63	−4.58	−4.61
NiAl:			
B2	−4.52	−4.38	−4.50
L1 <sub>0</sub>	−4.44	−4.36	−4.41
B32	−4.33	−4.25	−4.38
B20	−4.35	−4.27	−4.33
L1 <sub>1</sub> <sup>d</sup>	−4.33	−4.30	−4.25
B1 <sup>d</sup>	−3.96	−3.98	−3.85

<sup>a</sup> [23],<sup>b</sup> [24],<sup>c</sup> Calculated with ideal  $c/a = \sqrt{2}$  and a volume corresponding to equilibrium B2–NiAl structure,<sup>d</sup> Relaxed with respect to the unit cell volume, all internal atomic positions and fixed unit cell shape.

is stretched along the [00 1] direction and compressed in the [1 0 0] and [0 1 0] directions to keep a constant volume. When the  $c/a$  ratio of the tetragonal lattice changes from 1 to  $\sqrt{2}$ , the lattice structure changes from B2 to L1<sub>0</sub>. The second deformation path is obtained by stretching the B2 lattice along the [1 1 1] direction with a constant volume. When the angles of any two axes are 90°, 60° and 33.56°, the corresponding structures are B2, B1 and L1<sub>1</sub>, respectively. The energies of NiAl along the two deformation paths are shown in figure 9. It can be seen from figure 9 that the energies of the B1, L1<sub>1</sub> and L1<sub>0</sub> structures do not correspond to an energy minimum, which is in agreement with the first-principles results [28].

## 5. Conclusions

A potential suitable for studying the effect of Re on the  $\gamma$  (Ni)/ $\gamma'$  (Ni<sub>3</sub>Al) superalloy has been constructed based on experiments and first-principles calculations. The following conclusions are drawn.

- (1) The present potential gives an accurate fit to the basic lattice properties of pure Ni, Al, Re and Ni<sub>3</sub>Al. It is necessary to consider the inner elastic constants in the fitting of elastic constants of Re. The point defect properties of Ni and Ni<sub>3</sub>Al calculated with the present potential are also in reasonable agreement with experiments. The stacking fault energy of Ni and the planar fault energies of Ni<sub>3</sub>Al calculated with the present potential are in reasonable agreement with the experimental values.
- (2) The properties calculated with EAM potential are controlled by both the embedding energy and pair potential. However, the effect of embedding energy may be underestimated in the numerical fitting, such as the planar fault energies of Ni<sub>3</sub>Al. Some special fitting strategies are needed to reveal the effect of embedding energy. In this work, the effect of embedding energy on the properties of the alloys can be revealed by considering the relationship between the charge transfer calculated from first principles, the elastic constants of Ni<sub>3</sub>Al and the host electron density of EAM. The planar fault energies and cross-slip driving force in Ni<sub>3</sub>Al are improved by the above consideration.

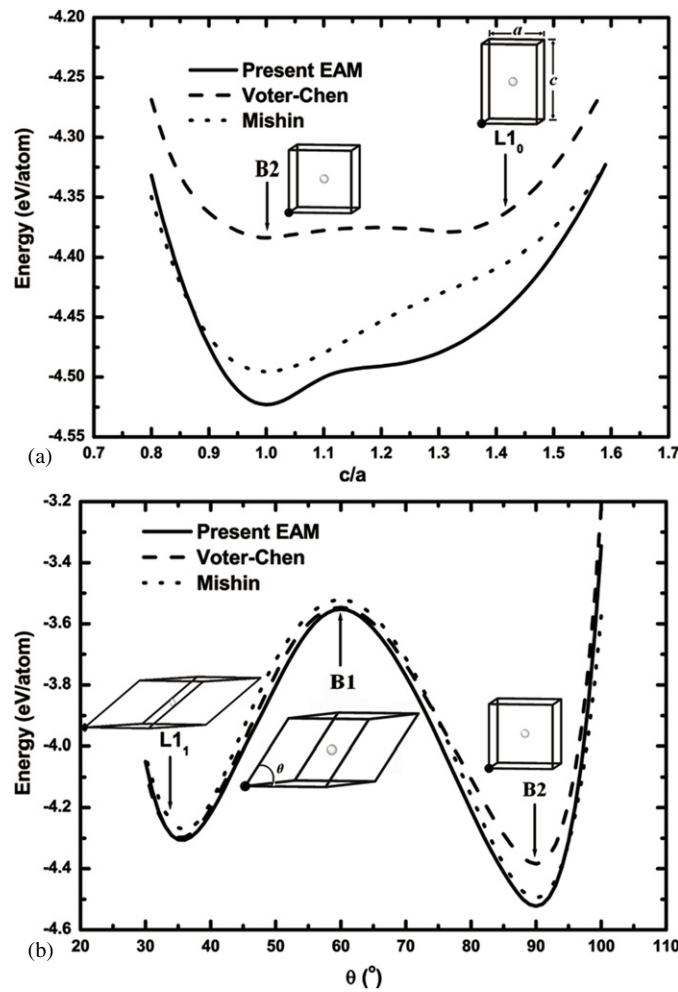


**Figure 9.** Energies of NiAl along deformation paths (a) from B2 structure to L1<sub>0</sub> structure and (b) from B2 structure to B1 and L1 structures. The volumes are kept to be the equilibrium volume of the B2 structure.

- (3) The present potential predicted that Re atoms do not form clusters in  $\gamma(\text{Ni})$ , which is consistent with experiments and first-principles calculations. We also investigated the effects of the alloying element Re on the lattice misfit of the  $\gamma(\text{Ni})$  and  $\gamma'(\text{Ni}_3\text{Al})$  systems, and the results were in agreement with first-principles calculations. The interaction energies between Re and the misfit dislocations of  $\gamma(\text{Ni})/\gamma'(\text{Ni}_3\text{Al})$  interface were calculated at 0 K, and the results showed that the Re atom could be a resistant solute to the misfit dislocations on the  $\gamma(\text{Ni})/\gamma'(\text{Ni}_3\text{Al})$  interface.

### Acknowledgments

The authors thank Professor J Cai for helpful discussions. This work was supported by the National Basic Research Program of China (Grant No 2011CB606402) and the National Natural Science Foundation of China (Grant No 51071091).

## References

- [1] Cetel A D and Duhl D N 1988 *Superalloys 1988* (Warrendale, PA: The Metallurgical Society) p 235
- [2] Giamei A F and Anton D L 1985 *Metall. Trans. A* **16** 1997
- [3] Broomfield R W, Ford D A, Bhangu H K, Thomas M C, Frasier D J, Burkholder P S, Harris K, Erickson G L and Wahl J B 1997 *Rhenium and Rhenium Alloys* (Warrendale, PA: The Minerals, Metals & Materials Society) p 731
- [4] Wanderka N and Glatzel U 1995 *Mater. Sci. Eng. A* **203** 69
- [5] Warren P J, Cerezo A and Smith G D W 1998 *Mater. Sci. Eng. A* **250** 88
- [6] Rüsing J, Wanderka N, Czubyko U, Naundorf V, Mukherji D and Rösler J 2002 *Scr. Mater.* **46** 235
- [7] Mottura A, Miller M K and Reed R C 2008 *Superalloys 2008* (Warrendale, PA: The Minerals, Metals & Materials Society) p 891
- [8] Mottura A, Wu R T, Finnis M W and Reed R C 2008 *Acta Mater.* **56** 2669
- [9] Mottura A, Warnken N, Miller M K, Finnis M W and Reed R C 2010 *Acta Mater.* **58** 931
- [10] Chen K, Zhao L R and Tse J S 2003 *Phil. Mag.* **83** 1685
- [11] Peng P, Soh A K, Yang R and Hu Z Q 2006 *Comput. Mater. Sci.* **38** 354
- [12] Wang Y J and Wang C Y 2008 *J. Appl. Phys.* **104** 013109
- [13] Zhu T and Wang C Y 2005 *Phys. Rev. B* **72** 014111
- [14] Yashiro K, Naito M and Tomita Y 2002 *Int. J. Mech. Sci.* **44** 1845
- [15] Kohler C, Kizler P and Schmauder S 2005 *Mater. Sci. Eng. A* **400–401** 481
- [16] Xie H X, Wang C Y and Yu T 2009 *Modelling Simul. Mater. Sci. Eng.* **17** 055007
- [17] Wu W P, Guo Y F, Wang Y S, Mueller R and Gross D 2011 *Phil. Mag.* **91** 357
- [18] Mottura A, Finnis M W and Reed R C 2012 *Acta Mater.* **60** 2866
- [19] Zhu T, Wang C Y and Gan Y 2010 *Acta Mater.* **58** 2045
- [20] Daw M S and Baskes M I 1983 *Phys. Rev. Lett.* **50** 1285
- [21] Daw M S and Baskes M I 1984 *Phys. Rev. B* **29** 6443
- [22] Foiles S M and Daw M S 1987 *J. Mater. Res.* **2** 5
- [23] Voter A F and Chen S P 1987 *Mater. Res. Soc. Symp. Proc.* **82** 175
- [24] Mishin Y 2004 *Acta Mater.* **52** 1451
- [25] Purja Pun G P and Mishin Y 2009 *Phil. Mag.* **89** 3245
- [26] Cai J and Ye Y Y 1996 *Phys. Rev. B* **54** 8398
- [27] Johnson R A 1989 *Phys. Rev. B* **39** 12554
- [28] Mishin Y, Mehl M J and Papaconstantopoulos D A 2002 *Phys. Rev. B* **65** 224114
- [29] Delley B 1990 *J. Chem. Phys.* **92** 508
- [30] Delley B 1991 *J. Chem. Phys.* **94** 7245
- [31] Banerjee A and Smith J R 1988 *Phys. Rev. B* **37** 6632
- [32] Johnson R A 1990 *Many-Atom Interactions in Solids* vol 48 (Berlin: Springer) p 85
- [33] Jones J E 1924 *Proc. R. Soc. Lond. A* **106** 463
- [34] Morse P M 1929 *Phys. Rev.* **34** 57
- [35] Rifkin J 2002 *XMD Molecular Dynamics Program* University of Connecticut, Storrs, CT (<http://xmd.sourceforge.net/>)
- [36] Plimpton S 1995 *J. Comput. Phys.* **117** 1
- [37] Dongare A M, Neurock M and Zhigilei L V 2009 *Phys. Rev. B* **80** 184106
- [38] Daw M S 1989 *Phys. Rev. B* **39** 7441
- [39] Hirshfeld F L 1977 *Theor. Chim. Acta* **44** 129
- [40] Iotova D, Kioussis N and Lim S P 1996 *Phys. Rev. B* **54** 14413
- [41] Kresse G and Hafner J 1993 *Phys. Rev. B* **47** 558
- [42] Kresse G and Furthmüller J 1996 *Phys. Rev. B* **54** 11169
- [43] Sheng H W, Kramer M J, Cadien A, Fujita T and Chen M W 2011 *Phys. Rev. B* **83** 134118
- [44] Kittel C 1976 *Introduction to Solid State Physics* (New York: Wiley)
- [45] Smithells C J (ed) 1976 *Metals Reference Book* (London: Butterworths)
- [46] Simmons G and Wang H 1971 *Single Crystal Elastic Constants and Calculated Aggregate Properties: A Handbook* (Cambridge, MA: MIT Press)
- [47] Weast R C (ed) 1984 *Handbook of Chemistry and Physics* (Boca Raton, FL: CRC Press)
- [48] Mauer F A, Munro R G, Piermarini G J, Block S and Dandekar D P 1985 *J. Appl. Phys.* **58** 3727
- [49] Hultgren R, Desai P D, Hawkins D T, Gleser M and Kelley K K 1973 *Selected Values of the Thermodynamic Properties of Binary Alloys* (Metals Park, OH: ASM)
- [50] Barrett C S and Massalski T B 1980 *Structure of Metals* (Oxford: Pergamon)

- [51] Brandes E A and Brook G B (ed) 1992 *Smithells Metal Reference Book* (Oxford: Clarendon)
- [52] Van Midden H J P and Sasse A G B M 1992 *Phys. Rev. B* **46** 6020
- [53] Born M and Huang K 1954 *Dynamical Theory of Crystal Lattices* (Oxford: Clarendon)
- [54] Pasianot R and Savino E J 1992 *Phys. Rev. B* **45** 12704
- [55] Rose J H, Smith J R, Guinea F and Ferrante J 1984 *Phys. Rev. B* **29** 2963
- [56] Mishin Y, Farkas D, Mehl M J and Papaconstantopoulos D A 1999 *Phys. Rev. B* **59** 3393
- [57] Reed R C 2006 *The Superalloys: Fundamentals and Applications* (Cambridge: Cambridge University Press)
- [58] Wycisk W and Feller-Knipmeier M 1978 *J. Nucl. Mater.* **69–70** 616
- [59] Koehler J S 1970 *Vacancies and Interstitials in Metals* (Amsterdam: North-Holland)
- [60] Baskes M I and Johnson R A 1994 *Modelling Simul. Mater. Sci. Eng.* **2** 147
- [61] Balluffi R W 1978 *J. Nucl. Mater.* **69–70** 240
- [62] Frantz J <http://www.frantz.fi/software/g3data.php>
- [63] Mishin Y and Herzig Chr 2000 *Acta Mater.* **48** 589
- [64] Dasgupta A, Smedskjaer L C, Legnini D G and Siegel R W 1985 *Mater. Lett.* **3** 457
- [65] Wang T M, Shimotomai M and Doyama M 1984 *J. Phys. F: Met. Phys.* **14** 37
- [66] Debiaggi S B, Decorte P M and Monti A M 1996 *Phys. Status Solidi. b* **195** 37
- [67] Jiang C and Gleeson B 2006 *Scr. Mater.* **55** 433
- [68] Ma S, Carroll L and Pollock T M 2007 *Acta Mater.* **55** 5802
- [69] Murr L E 1975 *Interfacial Phenomena in Metals and Alloys* (Reading, MA: Addison-Wesley)
- [70] Rice J R 1992 *J. Mech. Phys. Solids* **40** 239
- [71] Legrand P B 1984 *Phil. Mag.* **B 49** 171
- [72] De Boer F R, Boom R, Mattens W C M, Miedema A R and Niessen A K 1988 *Cohesion in Metals: Transition Metal Alloys* (Amsterdam: North-Holland)
- [73] Tyson W R and Miller W A 1977 *Surf. Sci.* **62** 267
- [74] Hull D and Bacon D J 2001 *Introduction to Dislocations* (Oxford: Butterworth-Heinemann)
- [75] Karnthaler H P, Mühlbacher E T and Rentenberger C 1996 *Acta Mater.* **44** 547
- [76] Mryasov O N, Gornostyrev Y N, Van Schilfgaarde M and Freeman A J 2002 *Acta Mater.* **50** 4545
- [77] Schoeck G, Kohlhammer S and Fahnle M 1999 *Phil. Mag. Lett.* **79** 849
- [78] Neumeier S, Pyczak F and Göken M 2008 *Superalloys 2008* (Warrendale, PA: The Minerals, Metals & Materials Society) p 109
- [79] Carroll L J, Feng Q, Mansfield J F and Pollock T M 2007 *Mater. Sci. Eng. A* **457** 292
- [80] Sato A, Harada H, Yeh A and Kawagishi K 2008 *Superalloys 2008* (Warrendale, PA: The Minerals, Metals & Materials Society) p 131
- [81] Zhang J X, Wang J C, Harada H and Koizumi Y 2005 *Acta Mater.* **53** 4623
- [82] Wang Y J and Wang C Y 2009 *Mater. Res. Soc. Symp. Proc.* **1224** FF05-31
- [83] Nabarro F R N and De Villiers H L 1995 *The Physics of Creep: Creep and Creep-Resistant Alloys* (London: Taylor and Francis)
- [84] Faken D and Jónsson H 1994 *Comput. Mater. Sci.* **2** 279
- [85] Lahrman D F, Field R D, Darolia R and Fraser H L 1988 *Acta Metall.* **36** 1309
- [86] Zhang J X, Murakumo T, Koizumi Y, Kobayashi T and Harada H 2003 *Acta Mater.* **51** 5073
- [87] Rusović N and Warlimont H 1977 *Phys. Status Solidi. a* **44** 609
- [88] Veyssi re P 1998 *Intermetallics* **6** 587
- [89] Paxton A T and Sun Y Q 1998 *Phil. Mag. A* **78** 85
- [90] Veyssi re P 2001 *Mater. Sci. Eng. A* **309–310** 44
- [91] Yoo M H 1986 *Scr. Metall.* **20** 915
- [92] Zener C 1948 *Elasticity and Anelasticity of Metals* (Chicago: University of Chicago)
- [93] Parthasarathy T A and Dimiduk D M 1996 *Acta Mater.* **44** 2237